Cell Biology:

The Bacterial Actin MamK : IN VITRO ASSEMBLY BEHAVIOR AND FILAMENT ARCHITECTURE

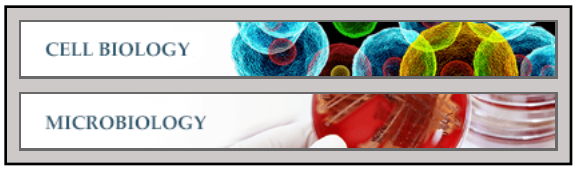

Ertan Ozyamak, Justin Kollman, David A. Agard and Arash Komeili

J. Biol. Chem. 2013, 288:4265-4277.
doi: 10.1074/jbc.M112.417030 originally published online November 30, 2012

THE JOURNAL OF BIOLOGICAL CHEMISTRY VOL. 288, NO. 6, pp. 4265–4277, February 8, 2013

The Bacterial Actin MamK

IN VITRO ASSEMBLY BEHAVIOR AND FILAMENT ARCHITECTURE[*] [S]

Received for publication, September 5, 2012, and in revised form, November 26, 2012 Published, JBC Papers in Press, November 30, 2012, DOI 10.1074/jbc.M112.417030

Ertan Ozyamak[‡], **Justin Kollman**[§], **David A. Agard**[¶], **and Arash Komeili**[‡1]

From the [‡]*Department of Plant and Microbial Biology, University of California, Berkeley, California 94720, the* [§]*Department of Anatomy and Cell Biology, McGill University, Montreal, Quebec H3A 2B2, Canada, and the* [¶]*Department of Biochemistry and Biophysics, University of California, San Francisco, California 94158*

Background: The bacterial actin MamK is involved in the organization of bacterial organelles called magnetosomes.
Results: MamK is an ATPase and assembles into filaments with a unique architecture.
Conclusion: MamK shares features of structure and assembly with other bacterial actin homologs, and it has some unique features of its own.
Significance: This work will guide future studies to unravel molecular mechanisms underlying MamK function *in vivo*.

It is now recognized that actin-like proteins are widespread in bacteria and, in contrast to eukaryotic actins, are highly diverse in sequence and function. The bacterial actin, MamK, represents a clade, primarily found in magnetotactic bacteria, that is involved in the proper organization of subcellular organelles, termed magnetosomes. We have previously shown that MamK from *Magnetospirillum magneticum* AMB-1 (AMB-1) forms dynamic filaments *in vivo*. To gain further insights into the molecular mechanisms that underlie MamK dynamics and function, we have now studied the *in vitro* properties of MamK. We demonstrate that MamK is an ATPase that, in the presence of ATP, assembles rapidly into filaments that disassemble once ATP is depleted. The mutation of a conserved active site residue (E143A) abolishes ATPase activity of MamK but not its ability to form filaments. Filament disassembly depends on both ATPase activity and potassium levels, the latter of which results in the organization of MamK filaments into bundles. These data are consistent with observations indicating that accessory factors are required to promote filament disassembly and for spatial organization of filaments *in vivo*. We also used cryo-electron microscopy to obtain a high resolution structure of MamK filaments. MamK adopts a two-stranded helical filament architecture, but unlike eukaryotic actin and other actin-like filaments, subunits in MamK strands are unstaggered giving rise to a unique filament architecture. Beyond extending our knowledge of the properties and function of MamK in magnetotactic bacteria, this study emphasizes the functional and structural diversity of bacterial actins in general.

Research over the last couple of decades has demonstrated that bacteria are not devoid of subcellular organization and that fine-tuned cellular processes govern their growth and development. Much of the appreciation for the level of complexity in bacteria has come with the discovery of homologs of the eukaryotic cytoskeletal proteins actin, tubulin, and intermediate filaments in bacteria (reviewed in Refs. 1–3). As in eukaryotes, these fulfill vital functions for cell growth, DNA segregation, and cell shape determination in bacteria.

Actin, one of the most abundant proteins in eukaryotes, is critical for many cellular functions (4, 5). It shows a remarkable level of sequence conservation across eukaryotic species (6, 7). In contrast, bacterial actin sequences are highly divergent and share only little primary sequence similarity to actin. Recent bioinformatic analysis suggests that there are more than 40 different families of bacterial actins (8). A unifying characteristic of actin and bacterial actins is the actin-fold, a conserved core structure that creates a nucleotide-binding and hydrolysis site (9, 10). One of the key features of actin is its ability to transition between monomeric and filamentous states. One of the main factors regulating this transition is the hydrolysis of nucleotides such as ATP by filamentous actin where hydrolysis provides an energy source for a conformational switch (4, 9, 10). In addition, a large number of accessory protein factors can influence this transition.

Similar to actin, bacterial actins form filamentous structures, and the majority of studies thus far have concentrated on a few select groups, such as the functionally distinct MreB and ParM proteins (11, 12). MreB is widely conserved and functions in cell shape determination in rod-shaped bacteria. Through its interaction with cell membrane and cell wall-associated proteins, it influences new cell wall synthesis (13). Recent *in vivo* studies suggest that MreB forms highly dynamic structures along the inner membrane of cells (14–16). It is unclear to what level MreB filament assembly and disassembly is a factor in *in vivo* MreB dynamics. ParM functions in the efficient segregation of low copy plasmids between daughter cells. ParM filaments exhibit dynamic instability *in vitro*, *i.e.* assembly and rapid catastrophic disassembly, that is distinct from the behavior of actin and is more microtubule-like (17). This dynamic behavior is important for ParM function because it provides a mechanism to "scan" for the plasmid. Upon "finding" the plasmid, by binding the ParR-*parC* complex, ParM filaments are stabilized, and their behavior transitions from dynamic instability to steady

* This work was supported, in whole or in part, by National Institutes of Health Grants R01GM084122 (to A. K.) and GM031627 (to D. A. A.). This work was also supported by a Howard Hughes Medical Institute grant (to D. A. A.).
[S] This article contains supplemental Figs. S1–S11.
[1] To whom correspondence should be addressed: Dept. of Plant and Microbial Biology, 261 Koshland Hall, Berkeley, CA 94720. Tel.: 510-642-2140; Fax: 510-642-4995; E-mail: komeili@berkeley.edu.

filament growth, enabling active movement of the plasmid (18). Although research on MreB and ParM has provided molecular and mechanistic insights into the function of these proteins, the function and properties of the majority of bacterial actins remain unexplored. However, it is becoming increasingly evident that the considerable sequence diversity within bacterial actins translates into functional, structural, and behavioral differences. Here, we performed a detailed analysis of the *in vitro* properties of the bacterial actin MamK from *Magnetospirillum magneticum* AMB-1, hereafter referred to as AMB-1.

MamK proteins form their own phylogenetic group within the bacterial actins and have been implicated in the organization of subcellular organelles in magnetotactic bacteria (19, 20). This phylogenetically diverse group of bacteria can form intracellular structures called magnetosomes, which are inner membrane invaginations that direct the formation of magnetic crystals. A single cell contains a number of magnetosomes that are aligned into one or multiple chains in the cytoplasm that together act as a compass needle. The possession of a magnetosome chain results in passive alignment of the bacteria to geo-magnetic field lines, which is thought to make the search for optimal growth conditions more efficient (21–23). The alignment of magnetosomes into well organized chains is dependent on MamK, and high resolution electron cryotomography studies have revealed that MamK likely forms filaments that flank magnetosomes *in vivo* (20, 24). Although genetic evidence suggests a role for MamK in magnetosome alignment, it is yet unknown if MamK filaments function in the establishment or the maintenance of a proper magnetosome chain. A study in the related organism *Magnetospirillum gryphiswaldense* MSR-1 suggests a role for MamK in the active positioning of magnetosomes during cell division (24). We recently demonstrated, using fluorescence recovery after photobleaching assays, that MamK-GFP forms dynamic filaments *in vivo*. Furthermore, an intact nucleotide-binding site and two redundant proteins, MamJ and LimJ, regulate filament dynamics *in vivo* (19).

To ultimately understand the role of MamK in cells, both *in vivo* and *in vitro* insights into MamK behavior is highly desirable. Several groups have previously studied the *in vitro* behavior of recombinantly expressed MamK. In an important first study, Taoka *et al.* (25) demonstrated that recombinant MamK can form filamentous structures *in vitro*. Filamentous bundles could be visualized by EM upon addition of ATPγS,[2] a nonhydrolyzable ATP analog, but not upon addition ATP, suggesting that MamK filaments disassembled prior to visualization due to ATP hydrolysis. Similar observations were made by Sonkaria *et al.* (26). In contrast, Rioux *et al.* (27) reported that MamK filament assembly occurred in the absence of ATP. These earlier studies presented valuable new insights; however, they provided only limited, and somewhat contradicting, information about assembly and filament dynamics and the role of nucleotides for MamK. Furthermore, these studies employed His-tagged derivatives of MamK that could exhibit different *in vitro* properties than the native untagged protein.

[2] The abbreviations used are: ATPγS, adenosine 5′-*O*-(thiotriphosphate); TIRF, total internal reflection fluorescence microscopy.

Here, we concentrated our efforts toward a more complete understanding of the *in vitro* properties and behavior of MamK. This is the first in-depth analysis of the assembly and filament architecture of an untagged MamK protein. We show that MamK assembles into filaments in an ATP-dependent manner and that filament disassembly occurs with very slow kinetics in low salt conditions. Near physiological levels of potassium or mutations in the protein's ATPase active site of the protein abolish this disassembly behavior. These results substantiate a model in which MamK filaments, unlike the inherently unstable bacterial actin ParM, are stable in their default state and require accessory factors to become dynamic. Moreover, we show by cryoelectron microscopy (cryo-EM) that MamK assembles into filaments with unique features, further highlighting the structural diversity of bacterial actins.

EXPERIMENTAL PROCEDURES

Expression and Purification of MamK—The *mamK* gene was amplified from genomic DNA of *M. magneticum* AMB-1 using a primer set that enabled the cloning of the gene into a pET29a vector using NdeI and HindIII restriction sites (forward primer, GCCATATGAGTGAAGGTGAAGGCC; reverse primer, CAAGCTTACGAGCCGGAGACGTCTC), creating MamK expression plasmid pAK420 (KanR). This plasmid was used as a template for site-directed mutagenesis to create mutant $MamK^{E143A}$ (pAK598) (forward primer, GCCCTAGTGGTGTCCGCCCCGTTCATGGTCGGC; reverse primer, GCCGACCATGAACGGGGCGGACACCACTAGGGC).
Sequences of plasmids were verified, and plasmids were transformed into *Escherichia coli* BL21(DE3) cells that already contained plasmid pLysS (CmR) encoding for T7 lysozyme to lower the background expression levels. Transformants were selected on LB medium in the presence of both kanamycin (50 μg/ml) and chloramphenicol (10 μg/ml). For MamK expression, cells were grown overnight in LB medium in the presence of both antibiotics at 30 °C. Overnight cultures were diluted into fresh medium to a starting of $OD_{650\ nm}$ ~0.05 and grown to $OD_{650\ nm}$ ~0.6, and isopropyl β-D-1-thiogalactopyranoside was added to a final concentration of 0.5 mM, cultures were incubated at 20 °C overnight. Cells were harvested and washed with ice-cold phosphate-buffered saline, pH 7.5, and pellets were frozen at −80 °C. Cell pellets were thawed and resuspended in ice-cold lysis buffer (10 mM Tris-HCl, pH 7.4, 25 mM KCl, 2 mM EDTA, 2 mM dithiothreitol (DTT)) processed through a French press, and cell debris was removed at 12,000 × *g* for 20 min. Ammonium sulfate cuts at 20% saturation were taken, and precipitates were resuspended in depolymerization buffer (10 mM Tris-HCl, pH 7.4, 25 mM KCl, 10 mM EDTA, 2 mM DTT) and incubated for 30 min. Subsequently protein was ultracentrifuged at 115,000 × *g* for 1 h at 4 °C to remove MamK polymers and aggregates, and a second ammonium sulfate cut (20%) was performed on the supernatant. Protein was resuspended in ice-cold depolymerization buffer and dialyzed extensively into polymerization buffer (10 mM Tris-HCl, pH 7.4, 25 mM KCl, 10% glycerol; 5 mM β-mercaptoethanol was included for dialysis) at 4 °C for 8–10 h. The glycerol level was adjusted to 30%, and protein aliquots were flash-frozen in liquid nitrogen and stored at −80 °C. The procedure described above yields highly

pure MamK protein samples, and we routinely employed this purification protocol. For nucleotide hydrolysis assays, we additionally gel-filtered MamK over a Superdex 200 matrix equilibrated in polymerization buffer. The presence of glycerol during the purification procedure and during experiments was necessary because we experienced that MamK frequently aggregated in its absence, especially in higher ionic strength buffers and at high protein concentrations. To perform experiments, MamK samples were thawed on ice, and the buffer was exchanged with G25 gel filtration resin (PD10 or Nap5 columns) equilibrated with polymerization buffer without reducing reagents. concentrations were calculated using a calculated molar extinction coefficient of 18,910 M^{-1} cm^{-1} at $A_{280\,nm}$. DTT was added to MamK samples to a final concentration of 1 mM, and samples were ultracentrifuged at 115,000 × *g* for 1 h at 4 °C prior to experiments. Various other buffers were used in this study as detailed under "Results."

Electron Microscopy—Negative stain EM samples were prepared by applying polymerized MamK to carbon-coated grids after glow-discharging, washing away unbound sample with water, and staining with 0.75% uranyl formate (28). Negative stain EM was performed on a Tecnai T12 Spirit LaB6 microscope (FEI Co.) operating at 120 kV, and images were acquired on a 4k × 4k CCD camera (Gatan, Inc.). Cryo-EM samples were prepared by applying polymerized MamK to glow-discharged C-FLAT holey-carbon grids, blotting in a Vitrobot (FEI Co.), and rapidly plunging into liquid ethane. A preliminary cryo-EM data set was obtained on a Tecnai F20 with a field emission gun operating at 200 kV with an 8k × 8k CCD camera (Tietz, Inc.) with a pixel size of 0.94 Å/pixel. The preliminary data set was used for determining helical symmetry parameters and testing for parallel *versus* antiparallel orientation of the two strands. The data used in the final reconstruction was obtained on a Titan Krios operating at 200 kV with a 4k × 4k Gatan Ultrascan camera with a pixel size of 1.09 Å/pixel. Total electron dose was in the range of 25–30 $e^-/Å^2$, and images were acquired over a defocus range of −1.4 to −3.5 μm (average −2.5 μm).

Image Processing—Defocus parameters for each micrograph were determined with CTFFIND (29). Contrast transfer function correction was achieved by applying a Wiener filter to the entire micrograph. Relatively straight lengths of helix were defined in the boxer program of the EMAN software suite (30). Preliminary reconstructions were determined by iterative helical real space reconstruction, performed essentially as described by Egelman (31) and Sasche *et al.* (32), using SPIDER (33) for projection matching and back projection, and the programs hsearch_lorentz and himpose (34). In all cases, a low pass filtered featureless cylinder was used as the initial model. The dataset used for initial characterization had a total of 11,476 overlapping segments, ~480 Å long, which included ~23,400 unique MamK subunits. Several independent reconstructions were calculated starting with different initial symmetry parameters, and in each case the helical symmetry converged to 23.4° azimuthal rotation and 53.1 Å axial rise per helical repeat (supplemental Fig. S10*C*). A second dataset was collected that included 7936 overlapping helical segments, ~370 Å long, which contained ~31,744 unique MamK subunits. The images were binned 2-fold for the reconstruction, with a final pixel size of 2.18 Å/pixel. In this case, 30 rounds of reconstruction were calculated with SPIDER as described above, followed by five rounds of refinement using the ihrsr routines in SPARX (35). Visualization of the cryo-EM reconstructions, fitting of the MamK homology model, and figure generation were performed with Chimera (36). Reference-free classification and averaging was carried out on images binned 4-fold, to 3.76 Å/pixel. The EMAN program startnrclasses was used for the classification (30).

Homology Modeling of MamK—A homology model of MamK was generated from the crystal structure of *Thermotoga maritima* MreB (Protein Data Bank code 1JCF) (37) using the program MODELLER (38). Several hundred sequences of MamK and MreB homologs were found by BLAST search (39), and a multiple sequence alignment was generated with all the sequences using MAFFT (40). The pairwise alignment between MamK and *T. maritima* MreB was extracted from the multiple sequence alignment and used as input for MODELLER.

Pelleting Assays—To assess MamK polymerization, protein samples were equilibrated to room temperature for 10 min before addition of nucleotide. Protein with nucleotide and control reactions were incubated at room temperature for 15 min, and the samples were spun at ~140,000 × *g* at room temperature in a Beckman Airfuge for 20 min. Supernatant and pellet fractions were recovered and analyzed by SDS-PAGE according to Laemmli (12% gels). Gels were stained with the GelCode Blue reagent (Thermo Scientific).

Light Scattering Assays—MamK bulk polymerization behavior was assessed by right angle light scattering on a Horiba Fluoromax-4 instrument with excitation and emission wavelengths set at 314 nm and a 0.5-nm slit width. Samples were equilibrated to room temperature for 5 min, and a stable light scattering signal was verified before the addition of 100 mM nucleotide stock solutions defined as t_0. Common to all measurements was a delay of ~4–6 s to manually mix the reactions before starting to record light scattering changes. All measurements were performed in triplicate unless stated otherwise, and all experiments of the same type were performed on the same day. To calculate critical concentrations, maximum intensity values were plotted against the protein concentration used in the assay (corrected for dilution), and the critical concentration was considered as the *x*-intercept in the plot. Maximum intensity values were derived from background subtracted data (intensity value at t_0) fitted with a sigmoidal function (Boltzmann) that described the data well (adjusted R^2 values >0.94).

Phosphate Release Assays—Release of inorganic phosphate (P_i) was quantitated using a coupled enzyme assay allowing continuous measurements (EnzCheck, Molecular Probes). The assay was based on the enzymatic conversion of substrate molecule MESG in the presence of P_i resulting in a product with a simultaneous shift of maximum absorbance to 360 nm. $A_{360\,nm}$ values were converted to P_i by using a phosphate standard. Reactions were performed using polymerization buffer specified above and not the buffer provided with the EnzCheck kit. Data were collected on an Ultrospec 2100 Pro spectrophotometer controlled by the SWIFT II software (GE Healthcare). All measurements were performed in triplicate.

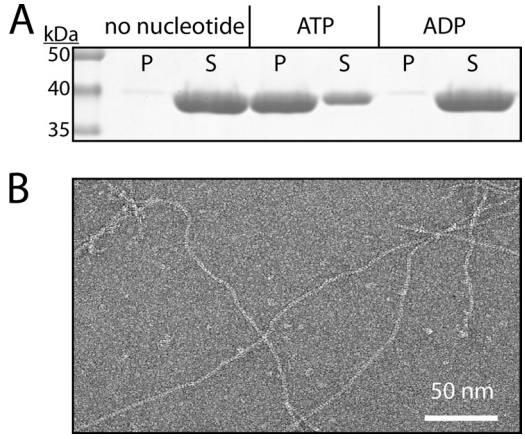

FIGURE 1. **MamK forms filaments in the presence of ATP.** *A,* MamK polymerizes in the presence of ATP but not ADP. MamK polymerization was assessed by pelleting assays as described under "Experimental Procedures;" pellet (*P*) and supernatant (*S*) fractions were analyzed. Nucleotide was added to MamK (40 μM) to a final concentration of 5 mM. Experiments were performed in the presence of 5 mM nucleotide and 1 mM $MgCl_2$; however, similar results were obtained in the presence of excess (2 mM nucleotide, 5 mM $MgCl_2$) or equimolar levels of $MgCl_2$ (5 mM nucleotide, 5 mM $MgCl_2$) (data not shown). *B,* negatively stained MamK filaments as visualized by transmission EM.

RESULTS

MamK Assembles into Filaments in an ATP-dependent Manner—Similar to eukaryotic actin, for bacterial actins the nucleotide state (NTP or NDP) of the protein was central for understanding their assembly and dynamics. Previous studies on MamK-His provided somewhat contradictory information about the role of nucleotides on MamK behavior. For our studies, we recombinantly expressed MamK from AMB-1 in *E. coli* cells and employed a purification strategy that does not require any affinity purification tags and yields large amounts of pure MamK protein (up to 25 mg/liter of stationary *E. coli* culture, see supplemental Fig. S1*A*). We first assessed the role of ATP and ADP for wild type MamK polymerization using pelleting assays. MamK in polymerization buffer (10 mM Tris-HCl, pH 7.4, 25 mM KCl, 10% glycerol, 1 mM $MgCl_2$, 1 mM DTT) was incubated either in the absence or presence of nucleotide (5 mM), and the extent of polymerization was monitored through pelleting (for details see "Experimental Procedures"). In the absence of any nucleotide, MamK remained primarily in the soluble fraction (Fig. 1*A*). A small amount of protein was detected in the pellet fraction, which may be a low level of protein aggregation that was consistently observed when very high protein concentrations (40 μM here) were incubated at room temperature but not at 4 °C. The addition of ATP resulted in a large proportion of the protein being detected in the pellet fraction indicating that, consistent with the behavior of other bacterial actins, MamK undergoes ATP-dependent polymerization. In contrast, the addition of ADP did not lead to MamK polymerization (Fig. 1*A*). Different bacterial actins appear to behave differently with regards to ADP-induced polymerization. For instance, the ADP-induced polymerization of ParM is only favored at much higher protein concentrations than for ATP-induced polymerization (~100× higher) (17, 41). We were unable to obtain reliable data at protein concentrations higher than 40 μM due to what appeared to be protein aggregation as judged by the appearance of white flakes that settled over time.

EM micrographs of negatively stained MamK incubated with ATP confirmed that MamK indeed polymerized into filamentous structures (Fig. 1*B*). The data show that MamK can polymerize *in vitro* in the presence of ATP and that there maybe a high energetic barrier for polymerization with ADP.

Our purification trials and initial experiments indicated that divalent cations may be important for MamK filament stability. For instance, during purification the treatment of the ammonium sulfate fraction with high levels of EDTA was necessary to obtain unassembled MamK protein that remained in the supernatant after ultracentrifugation. To assess this behavior in more detail, we followed the level of MamK assembly in the presence or absence of EDTA by pelleting assays (supplemental Fig. S1*B*). We polymerized MamK by the addition of ATP and examined the level of unassembled MamK protein after extensive dialysis of samples in the presence or absence of EDTA. To account for protein aggregation, we also performed these experiments in parallel in the absence of ATP. As expected, the addition of ATP resulted in a significant decrease in the level of MamK in the supernatant due to filament formation and sedimentation during pelleting (supplemental Fig. S1*B*). The incubation of MamK filaments in the absence of EDTA did not result in higher levels of soluble MamK in the supernatant (supplemental Fig. S1*B*). In contrast, the polymerized MamK sample that was dialyzed against buffer containing 5 mM EDTA disassembled as evidenced by the increase of protein in the supernatant. Furthermore, this disassembled protein was competent to undergo a second round of polymerization when EDTA was removed (supplemental Fig. S1*B*). The influence of EDTA on MamK filament formation indicates that divalent cations are important for filament stability.

MamK Filament Assembly Is Rapid in the Presence of ATP—The pelleting experiments above provide a static picture of MamK filament formation. Therefore, we used right angle light scattering to assess bulk assembly kinetics of MamK filaments in a dynamic fashion. Experiments were performed in the presence of saturating levels of nucleotide for a range of protein concentrations. In the presence of 5 mM ATP-$MgCl_2$, MamK assembly was rapid, and a steady state was reached within a few minutes when an initial protein concentration of ~12 μM protein was used (Fig. 2*A*). Similar to ParM (17, 41), the assembly curves could be described by an initial phase of rapid increase in light scattering intensity and a brief decrease before a steady state was reached (Fig. 2*A*). At lower protein concentrations, the decrease of intensity before steady state was not as apparent, and the time to reach steady state was prolonged. At ~2 μM, protein polymerization kinetics exhibited a long lag phase, and the data followed a sigmoidal function (supplemental Fig. S2). This suggests that MamK assembles via a nucleation-condensation mechanism as described for eukaryotic and other bacterial actins.

We also evaluated the polymerization kinetics of mutant $MamK^{E143A}$. Based on the ATP hydrolysis model for actin by Vorobiev *et al.* (42), this mutation is expected to be important for nucleotide hydrolysis, and the equivalent E148A mutation in ParM was shown to abolish the ATPase activity of ParM (17).

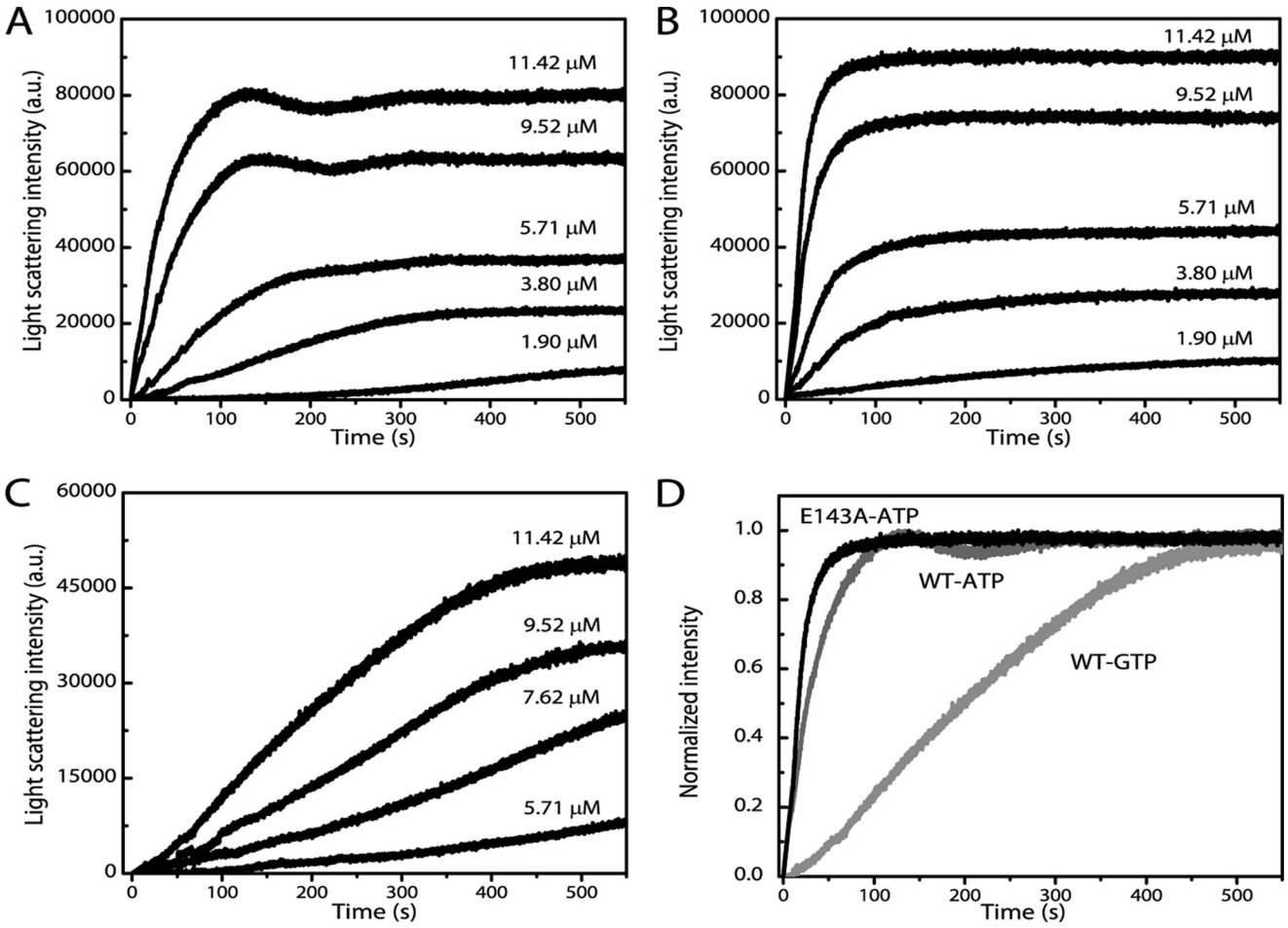

FIGURE 2. **MamK polymerization is rapid in the presence of saturating levels of ATP.** Wild type MamK (*A*) and mutant MamK^{E143A} (*B*) polymerization kinetics were assessed by light scattering assays in the presence of 5 mM ATP-$MgCl_2$. Initial polymerization kinetics appear faster for mutant MamK^{E143A} (nucleotide hydrolysis mutant). Polymerization with 5 mM GTP is not as rapid as with ATP (*C*); 5 mM $MgCl_2$ was present in the buffer prior to addition of GTP for experiments in *C*. ATP polymerization kinetics are identical to data in *A* when $MgCl_2$ is present before nucleotide addition (data not shown). *D,* normalized light scattering intensities at 11.42 μM protein concentration when MamK is polymerized with either ATP or GTP. *A–D,* each trace for a particular protein concentration is the average of three measurements on the same day.

Additionally, MamK^{E143A}-GFP has been shown to form static filaments *in vivo* (19). Similar to the wild type protein, mutant MamK^{E143A} polymerizes rapidly in the presence of saturating levels of ATP-$MgCl_2$ (Fig. 2*B*). Interestingly, polymerization curves for the mutant did not exhibit the three phases as the wild type protein, and the steady-state was reached immediately after initial rapid polymerization. In addition, there was no long lag phase apparent at the lowest protein concentration tested here.

Having established the role of ATP for MamK polymerization, we sought to determine whether and to what extent other nucleotide triphosphates can induce MamK polymerization. Eukaryotic and different bacterial actins appear to show distinct binding preferences and polymerization efficiencies with the purine nucleotide triphosphate, GTP (17, 41, 43–48). To address this question, we tested GTP-induced polymerization of MamK by light scattering assays. As can be seen in Fig. 2, *C* and *D*, MamK also polymerizes in the presence of GTP-$MgCl_2$; however, polymerization rates are lower than with ATP. The addition of 5 mM ADP-$MgCl_2$ to ~12 μM MamK did not lead to changes in light scattering intensities, again demonstrating that ADP, as in pelleting assays, does not induce MamK polymerization (data not shown).

In addition to providing insights about the kinetics/dynamics of filament assembly, light scattering data also allow the extraction of the critical concentration for polymerization. This is the minimal concentration of protein required for formation of nucleation seeds that can then transition into full filament assembly. We determined the critical concentration for the wild type protein to be ~0.7 μM when ATP was used (supplemental Fig. S3 and Table 1), a value similar to reported values for other bacterial actins (17, 41, 43–46). The critical concentration for mutant MamK^{E143A} was roughly half that of the wild type (~0.38 μM; supplemental Fig. S3 and Table 1). Garner *et al.* (17) reported a similar level of reduction of the critical concentration for ParM with the equivalent mutation. In the case of GTP, the lower efficiency of wild type MamK polymerization was concomitant with a roughly 3-fold higher critical concentration (~2.01 μM; supplemental Fig. S3 and Table 1) than with ATP. Together, these data show that MamK can efficiently nucleate *in vitro* to rapidly assemble into filaments in the presence of ATP.

TABLE 1
Critical concentration of MamK in the presence of different nucleotides

MamK	Nucleotide	Critical concentration
		μM
Wild type	ATP	0.69 ± 0.15
	ADP	>40
	GTP	2.01 ± 0.23
Wild type[a]	ATP	0.71 ± 0.1
E143A	ATP	0.38 ± 0.08

[a] This is in polymerization buffer with 75 mM KCl.

MamK Is an ATPase and Mutation E143A Largely Abolishes Its Activity—Actin and actin-like proteins share a common nucleotide-binding motif, and ATP hydrolysis is an important factor regulating disassembly of actin filaments. Here, we performed enzyme-coupled P_i release assays to examine and follow MamK's ATPase activity. We also assayed for the ATPase activity of mutant MamK^{E143A}. As mentioned above, the mutation of the conserved glutamate residue at position 143 is predicted to affect ATP hydrolysis. Continuous P_i release measurements were carried out under conditions that paralleled light scattering assays. When wild type MamK was incubated with 2 mM ATP-$MgCl_2$, P_i release was evident after a short lag phase and proceeded at a steady increase rate (Fig. 3*A*). Control experiments assessing apparent P_i release in the absence of ATP (only protein) and absence of protein (just ATP) did not show appreciable changes (data not shown). In contrast, in the presence of mutant MamK^{E143A} P_i release is not significant, and only ~5% of the wild type activity remained (Fig. 3*A*). The wild type activity increases linearly over a range of protein concentrations, whereas MamK^{E143A} activity remains low (Fig. 3*B*). MamK exhibited an ATPase activity of around 0.2 μM min^{-1}/μM protein. The data demonstrate that MamK can hydrolyze ATP and that mutation E143A largely abolishes its activity.

MamK Filaments Disassemble and Mutation E143A Affects Disassembly Kinetics—A key feature of actin and bacterial actins is the ability to transition between assembled and unassembled states. To evaluate the kinetics of filament disassembly of MamK, we again used light scattering assays. Previous experiments were performed in the presence of saturating levels of ATP; however, under these conditions disassembly events are not detected (we reasoned that disassembled subunits may quickly be recharged with ATP and reincorporated into the filaments). Thus, we performed polymerization experiments in the presence of significantly lower ATP levels (≤50 μM) with the rationale that after depletion of ATP in the reaction mixtures disassembly of MamK filaments might be observed. When MamK polymerization was induced with only 50 μM ATP-$MgCl_2$, wild type MamK still assembled rapidly, but the steady-state light scattering values and the maximal velocities were lower than when 2 mM ATP-$MgCl_2$ was used (187 ± 27 and 564 ± 39 light scattering units/s, respectively, see Fig. 4*A*). Intensity signals stayed stable for long periods of time but began to decay ~750 s after addition of ATP (± ~140 s) and returned to values seen before the addition of ATP indicating complete disassembly of wild type MamK filaments. No decay in light scattering intensities was observed in the presence of 2 mM ATP-$MgCl_2$ indicating that no bulk filament disassembly occurred within the duration of the experiments (2200 s). When polymerized with 20 μM ATP-$MgCl_2$, the initial rate of polymerization was even slower (106 ± 17 light scattering units/s) than with 50 μM ATP-$MgCl_2$. No plateau phase was observed this time, and intensity signals started to decay at earlier time points. Decay rates were lower than with 50 μM ATP-$MgCl_2$ (Fig. 4*A*; −40 ± 20 and −62 ± 22 light scattering units/s for 20 and 50 μM ATP-$MgCl_2$, respectively). The data show that even under ATP-limiting conditions MamK filaments have a slow bulk rate of filament disassembly. This stands in contrast to ParM, which under similar experimental conditions displays a rapid disassembly of filaments (17). We repeated the experiments above for mutant MamK^{E143A}. Interestingly, the mutant polymerized with similar maximal velocities irrespective of the ATP-$MgCl_2$ concentration used, reached similar maximal light scattering intensities, and, unlike wild type filaments, the intensity values remained stable (Fig. 4*B*).

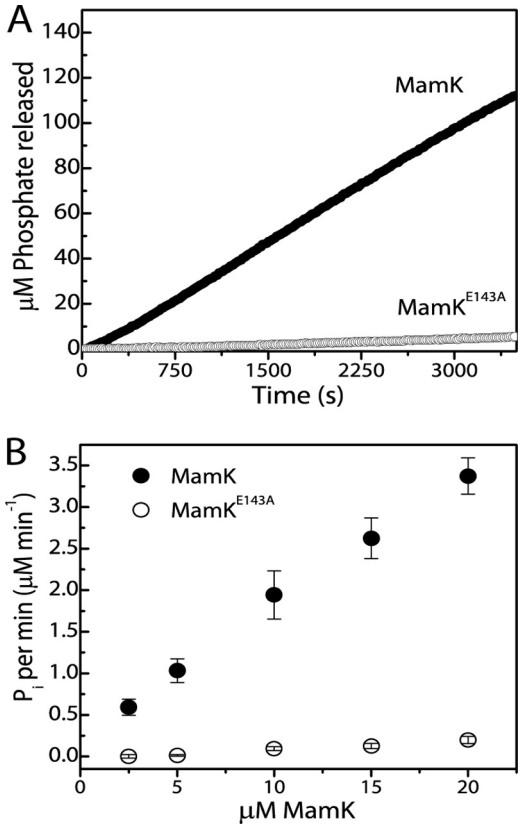

FIGURE 3. **MamK is an ATPase.** ATPase activity was inferred by measuring P_i released during the assay as described under "Experimental Procedures." *A,* 9.52 μM wild type MamK (*closed circles*) and mutant MamK^{E143A} protein (*open circles*) were polymerized in the presence of 2 mM ATP-$MgCl_2$, and P_i release was measured over time. MamK^{E143A} exhibits a much reduced ATPase activity (~5% of wild type activity). Each trace is the average of three measurements on the same day. *B,* P_i release over a range of protein concentrations. P_i release was assessed for wild type MamK and MamK^{E143A} 30 min after the addition of 2 mM ATP-$MgCl_2$. The average and standard deviations from three experiments are shown.

To correlate filament assembly/disassembly with ATPase activity, we performed light scattering and P_i release assays on the same day, using the same protein preparations for both assays. When polymerization was induced with 50 μM ATP-$MgCl_2$, P_i release started at a slow rate and increased as light scattering intensities approached a plateau phase, after which

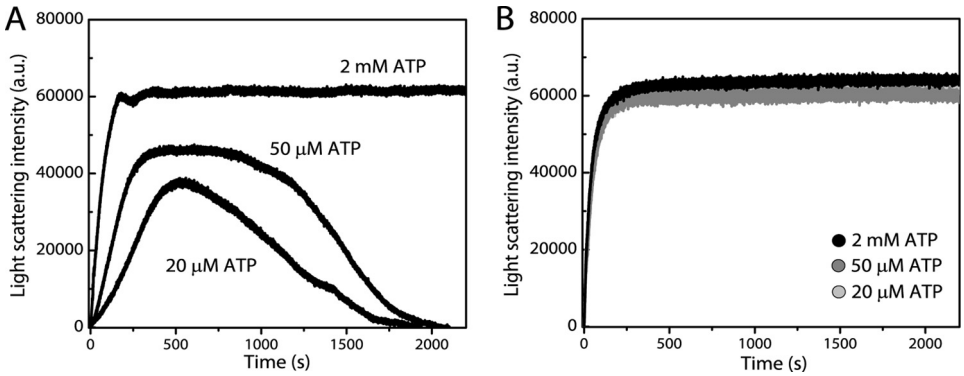

FIGURE 4. **Mutation E143A affects MamK filament disassembly.** Polymerization of 9.52 μM wild type MamK (*A*) and MamK^{E143A} (*B*) protein was assessed by light scattering assays in the presence of 25 and 50 μM and 2 mM ATP-$MgCl_2$. Wild type protein signals decayed with very slow kinetics indicating the lack of dynamic instability. MamK^{E143A} reaches the same maximal light scattering intensity at all ATP-$MgCl_2$ concentrations used and does not exhibit decay in light scattering intensities. Each trace for a particular protein concentration is the average of three measurements on the same day.

time it increased at a linear rate for the duration of the plateau phase in light scattering intensities (supplemental Fig. S5). The same behavior was observed in the presence of 2 mM ATP-$MgCl_2$ (data not shown). Interestingly, the start of the decay in light scattering intensities did not correlate with depletion of ATP and started while P_i release rate was still increasing linearly (supplemental Fig. S5). Again, in the presence of 50 μM ATP-$MgCl_2$, the MamK^{E143A} protein polymerized rapidly, and light scattering intensities remained stable, but no significant P_i release was seen (supplemental Fig. S5).

The data above imply that MamK^{E143A} subunits perform a round of assembly but fail to disassemble. To test this hypothesis further, we asked whether substoichiometric levels of MamK^{E143A} would affect wild type MamK filament disassembly kinetics. The underlying assumption is that disassembly occurs gradually starting at the ends of the filaments after ATP hydrolysis and a MamK-ATP subunit without ATP hydrolyzing activity could "cap" and prevent depolymerization. To address this question, we performed two different experiments. We initially mixed small amounts of mutant protein (~2.5 and ~ 5%) with ~10 μM wild type protein and monitored assembly and disassembly after addition of 20 μM ATP-$MgCl_2$. Control experiments with either wild type or mutant protein showed the expected behavior (supplemental Fig. S6*A*). However, introducing ~2.5% mutant protein into the reaction mixture significantly decreased the disassembly rate in duplicate experiments (supplemental Fig. S6*A*). In separate experiments where we kept the total protein concentration constant, a similar behavior was evident. With 90% wild type MamK and 10% MamK^{E143A} protein, the initial rate of increase in light scattering intensities was higher, and no decay in intensities was observed (supplemental Fig. S6*B*). These data suggest that the two proteins can potentially form mixed filaments and that MamK subunits that do not hydrolyze ATP may stabilize filaments. Taken together, the data suggest that mutation E143A in MamK, which abolishes ATPase activity, negatively affects filament disassembly but not filament assembly.

Potassium Levels Influence MamK Disassembly Characteristics—Our initial experiments were performed in the presence of 25 mM KCl mainly because protein purification was most successful at this concentration, and MamK protein was stable even at fairly high protein concentrations. However, K^+ is the most abundant cation in bacterial cells and is found inside cells at concentrations far higher than 25 mM (49–53). Therefore, we evaluated the influence of higher K^+ concentrations on MamK polymerization. Increasing KCl levels by even 3-fold, to 75 mM, appeared to significantly increase the maximal rate at which filaments assembled (Fig. 5*A*). In the presence of 75 mM KCl and 25 μM ATP-$MgCl_2$, the maximal assembly rate was roughly seven times higher than with 25 mM KCl (890 ± 56 and 122 ± 25 light scattering units/s, respectively). Notably, the assembly rate with 75 mM KCl and 25 μM ATP-$MgCl_2$ was similar to when saturating levels of ATP (2 mM) were added in the presence of 25 mM KCl. Interestingly, at 75 mM KCl, no bulk filament disassembly was observed, whereas with 25 mM KCl disassembly was evident (Fig. 5*A*). The further increase of KCl to 150 mM had no additional effect and showed similar behavior to that of 75 mM KCl (data not shown).

The above observed behavior with higher KCl concentrations is not due to increased levels of Cl^- ions because it is mirrored when KCl is replaced by potassium glutamate (Fig. 5*B*). The rapid polymerization and lack of disassembly of wild type MamK was similar to the behavior of the MamK^{E143A}. Hence, we tested whether wild type MamK's ATPase activity was reduced in the presence of 75 mM KCl. However, P_i release rates were similar at all KCl levels. In the presence of 2 mM ATP-$MgCl_2$ and 75 mM KCl, P_i release rates were almost identical to those at 25 mM KCl, apart from the initial phase in which there appeared to be a small burst of P_i release followed by a phase of steady increase in P_i (supplemental Fig. S7*A*). Similarly, when 25 μM ATP-$MgCl_2$ was used, a faster initial P_i release was evident with 75 mM KCl (supplemental Fig. S7*B*). We also assessed polymerization in the presence of 75 mM KCl for a range of protein concentrations, and we determined the critical concentration to be unchanged (Table 1 and supplemental Fig. S3*D*).

Arguably, the observed behavior at higher K^+ levels could be due to an increased ionic strength of the buffer. To address this, we replaced KCl in the buffer by NaCl and attempted to look at efficiency of polymerization again using 25 μM ATP-$MgCl_2$. We did not detect any polymerization in buffer containing either 25 or 75 mM NaCl at this ATP-$MgCl_2$ concentration (data not shown), perhaps suggesting a lowered binding affinity of MamK for ATP. When we tested MamK polymerization at a

much higher ATP-$MgCl_2$ concentration of 500 μM in combination with 25 mM NaCl, nucleation appeared to be inefficient with a long lag phase (supplemental Fig. S8*B*). When 75 mM NaCl was present, nucleation and polymerization were faster but significantly slower than in the presence of 25 mM KCl (supplemental Fig. S8*B*). Polymerization in 75 mM NaCl buffer was comparable with polymerization in 25 mM KCl buffer when even higher levels of ATP-$MgCl_2$ were used (2 mM) (supplemental Fig. S8*A*). P_i release assays showed that MamK's ATPase activity was generally lower with NaCl. In relation to the activity at 25 mM KCl and 2 mM ATP-$MgCl_2$, the maximal velocity in the presence of 25 mM NaCl was only ~21 and ~43% with 75 mM NaCl (supplemental Fig. S8, *C* and *D*).

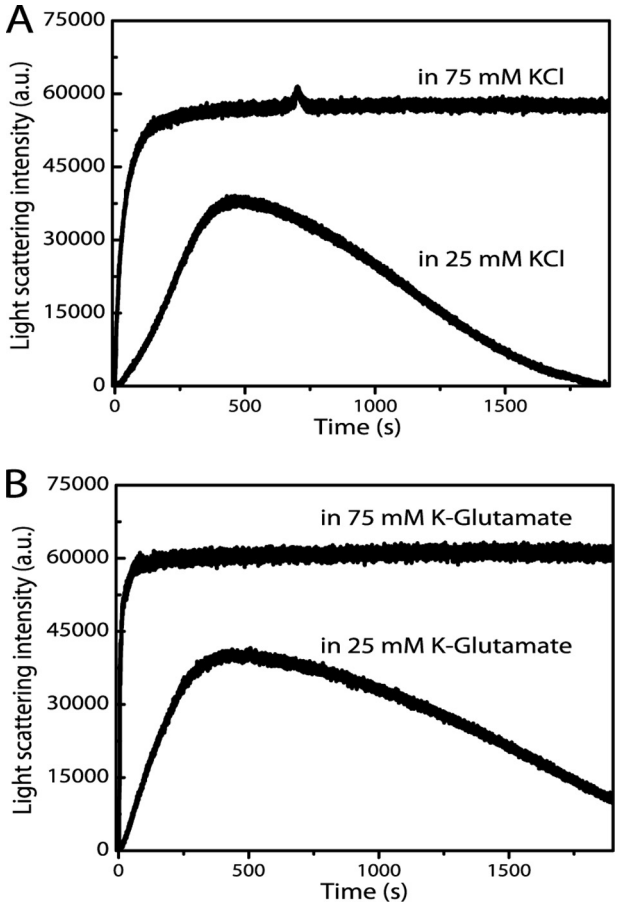

FIGURE 5. **MamK disassembly depends on potassium levels.** Decay of light scattering intensities was assessed for 9.52 μM MamK after polymerization with 25 μM ATP-$MgCl_2$ in polymerization buffer with either 25 or 75 mM KCl (*A*). Initial rates of polymerization were higher in the presence of 75 mM KCl, and no bulk depolymerization was observed. The effect is specific to potassium ions, and not chloride ions, because the behavior is similar in buffer with potassium glutamate (*B*). Each trace is the average of three measurements on the same day.

To further investigate the effect of potassium levels on MamK behavior, we imaged MamK filaments in the presence of different KCl levels by EM. MamK (5 μM) polymerization was induced with ATP-$MgCl_2$, and filaments were negatively stained for imaging. In the presence of 25 mM KCl, single MamK filaments were highly abundant (Fig. 6); however, with 75 mM KCl, some filament bundling was apparent. Strikingly, in the presence of 150 mM KCl MamK filaments clearly assembled into bundles (Fig. 6). This potassium-dependent bundling behavior was also dependent on the protein concentration, with similar levels of filament bundling occurring even at lower KCl concentrations provided the protein concentration was high enough. When 17 μM MamK was polymerized, filament bundles were highly abundant at even 75 mM KCl (data not shown). Bundles of filaments are likely to scatter more light than single filaments, and this may provide an explanation for the apparent, but misleading, increased bulk polymerization rates. Nonetheless, these data show that moderate changes in K^+ levels can inhibit MamK filament disassembly, possibly through inter-filament interactions, and not by inhibiting ATP hydrolysis.

Role of Magnesium for MamK Filament Stability—The divalent cation Mg^{2+} plays an important role for actin and actin-like protein because the physiological form of ATP in cells is an Mg-ATP chelate. Actin has a single high affinity binding site that is located in the ATP binding pocket and lower affinity sites located elsewhere (7). The vast majority of our experiments (with the exception of experiments in Fig. 1*A*) were performed in the presence of equimolar levels of ATP and $MgCl_2$. However, free magnesium could play an additional role for MamK assembly/disassembly; hence, we tested the effects of excess levels of Mg^{2+} ions.

We performed light scattering assays, with 9.52 μM MamK in the standard polymerization buffer containing 25 mM KCl, an we used 50 μM ATP and varying levels of $MgCl_2$ to induce MamK polymerization. A 10-fold excess of Mg^{2+} over ATP (50 μM ATP and 500 μM $MgCl_2$) did not result in a significantly different assembly and disassembly behavior as compared to when equimolar levels were used (50 μM ATP and 50 μM $MgCl_2$), although disassembly appeared to occur on average slightly slower (supplemental Fig. S9*A*). Interestingly, in the presence of 20-fold excess Mg^{2+} (50 μM ATP and 1000 μM $MgCl_2$) the initial rate of polymerization was higher, and light scattering intensities decayed at a reduced rate as compared to when equimolar levels of $MgCl_2$ and ATP were used (supple-

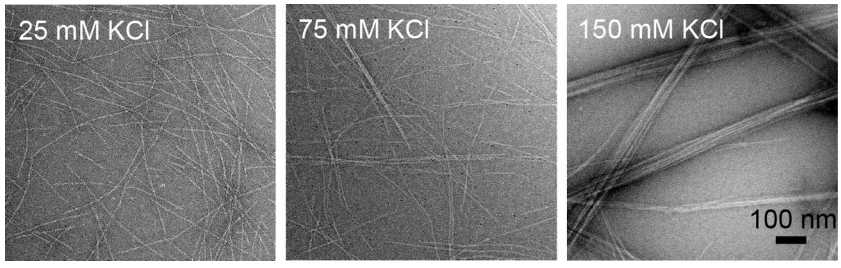

FIGURE 6. **MamK filaments assemble into bundles in a potassium-dependent manner.** EM micrographs of negatively stained MamK filaments in the presence of different KCl levels. 5 μM MamK was polymerized by addition of 5 mM ATP-$MgCl_2$. KCl levels are specified in micrographs.

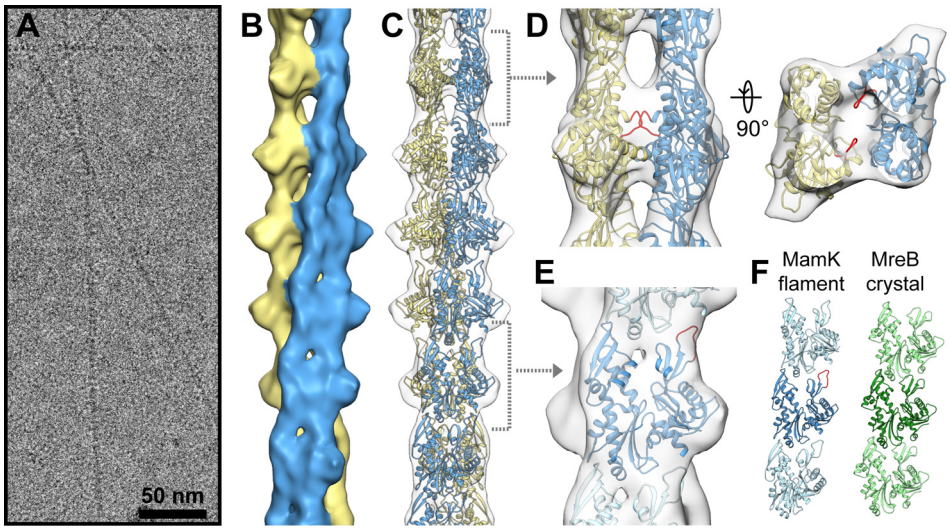

FIGURE 7. **Cryo-EM reconstruction of MamK filaments.** *A,* section of a micrograph of frozen MamK filaments. *B,* final three-dimensional reconstruction of the MamK filament rendered at 12 Å resolution, with each of the two strands shown in a different color. *C,* homology model of MamK fit into the cryo-EM reconstruction. *Dashed brackets* indicate regions shown in greater detail in *D* and *E*. *D,* contacts between strands are shown in the side view (*left*) and looking down the filament axis (*right*). Although precise residue interactions cannot be confidently predicted at this resolution, an insert unique to MamK (*red*) lies near the regions of strongest interaction and may play a role in forming the unique filament architecture. *E,* close-up view of a single MamK homology model fit into the cryo-EM density, with subdomains labeled. An insert unique to MamK, shown in *red*, is near the longitudinal contact surface and may play a role in the unique assembly dynamics of MamK. *F,* longitudinal contacts between MamK protomers (*blue*) are similar to the crystal-packing contacts of *T. maritima* MreB (*green,* Protein Data Bank code 1JCF). The central subunit in each strand is in the same orientation. Within the crystal MreB packing is linear, whereas a rotation of 23.3° between MamK subunits results in twisted strands.

mental Fig. S9*A*). In the presence of a 100-fold excess of Mg^{2+} (50 μM ATP and 5000 μM $MgCl_2$) no MamK filament disassembly could be observed (supplemental Fig. S9*A*). We also performed experiments in the presence of excess ATP over Mg^{2+} (500 μM ATP and 50 μM $MgCl_2$) resulting in stable light scattering signals (supplemental Fig. S9*B*) verifying that filament stability in the presence of saturating levels of ATP is distinct from the phenomenon seen with a great excess of Mg^{2+}.

We reasoned that the behavior in the presence of 100-fold excess of Mg^{2+} was similar to the behavior observed with increased K^+ levels, and hence we imaged the MamK filament after polymerization with 50 μM ATP and 5000 μM $MgCl_2$. Our analysis showed that, under these conditions, MamK formed single filaments, and not filament bundles as seen with increased K^+ levels (data not shown). Interestingly, ATP hydrolysis/P_i release was significantly reduced at steady state (supplemental Fig. S9*C*), perhaps partially explaining the lack of bulk depolymerization observed in these experiments (supplemental Fig. S9*A*). The data above are in agreement with the data presented in supplemental Fig. S1*B* and indicate that Mg^{2+} ions can influence MamK filament stability.

Cryo-EM Reconstruction of MamK Filaments—To provide a framework for understanding the assembly of MamK filaments, we determined their three-dimensional structure from cryo-electron micrographs (Fig. 7*A*). Two-dimensional reference-free class averages of MamK filaments suggested that, like actin and most bacterial actin homologs studied to date, MamK assembles into two-stranded helical filaments (Fig. 7*B*). But, unlike other actin-like filaments, which have staggered strands offset by half a subunit, the MamK strands are unstaggered (supplemental Fig. S11). A very similar pattern was seen recently in two-dimensional averages of MreB filaments assembled on lipid layers, although MreB filaments are straight rather than the twisted helical filaments of MamK (13).

In the average MreB images, the shapes of the subunits suggested to the authors that the two strands are antiparallel, raising the question of whether the two MamK strands are parallel or antiparallel. To generate a correct three-dimensional reconstruction of MamK, we had to first determine whether the strands were parallel or antiparallel so that the correct symmetry could be enforced. We tested the cross-strand symmetry by comparing a preliminary asymmetric reconstruction to reconstructions with parallel or antiparallel symmetry imposed. The asymmetric reconstruction closely resembled the reconstruction with parallel cross-strand symmetry imposed, with well defined subunits with the bi-lobed structure common among actin homologs. When antiparallel symmetry was imposed, however, the subunits lost their definition (supplemental Fig. S10*B*). These results suggested that the MamK strands are parallel leading us to impose parallel cross-strand symmetry in the final refinement.

The final structure, determined by iterative helical real space reconstruction, has a resolution of 12 Å, with refined helical symmetry of 23.4° azimuthal rotation and 53.1 Å axial rise (supplemental Fig. S10, *C* and *D*). To aid in interpreting the cryo-EM reconstruction, we generated a homology model of MamK from the crystal structure of *T. maritima* MreB (Protein Data Bank code 1JCF (37)). The subunit model fits well into the cryo-EM density with no significant clashing between subunits (Fig. 7, *C–E*). Although we did not determine the absolute hand of the MamK filament structure, it should be noted that the MamK subunit model only fit well into the right hand filament.

MamK subunits make longitudinal contacts along each strand using surfaces similar to those of F-actin (54–56), the

bacterial actin homolog ParM (57), and the filament-like crystal packing interactions of MreB (Fig. 7*F*) (37). A six-residue insertion of mostly hydrophobic residues in MamK relative to MreB is at the longitudinal contact site in domain Ib, positioned to make contacts with the base of domain Ia of an adjacent subunit (Fig. 7*E*, *red loops*). The D-loop of eukaryotic actin has a similar hydrophobic loop at this position involved in longitudinal contacts, suggesting that in this regard MamK polymerization may be more similar to actin than to MreB. Indeed, the azimuthal rotation and helical rise between subunits along each MamK strand are more similar to those of actin (supplemental Fig. S11).

Although the longitudinal contacts in the MamK filament are generally conserved with other actin homologs, the cross-strand contacts are completely novel, giving rise to the unique 2-fold point group symmetry between strands. The strongest cross-strand contacts are along the outer edges of each subunit, leaving a gap near the center of the helix (Fig. 7*D*). Given the uncertainty inherent in the homology model and the limited resolution of the cryo-EM reconstruction, it is difficult to predict the precise residues involved in these novel cross-strand contacts. However, a five-residue insertion unique to the MamK family lies in the linker between domains Ia and Ib, at a position very near the strongest contacts between the strands, suggesting this site may play a role in stabilizing the novel cross-strand contacts (Fig. 7*D*, *red loops*).

DISCUSSION

As opposed to their eukaryotic counterparts, bacterial actin sequences are highly divergent and fulfill a wide range of cellular functions. This sequence and functional diversity are also accompanied by differences in dynamics and filament architecture. In this study, we characterized the *in vitro* properties of the bacterial actin MamK from *M. magneticum* AMB-1, which is involved in the organization and positioning of organelles in magnetotactic bacteria. The two major findings of our study are as follows: (i) MamK filaments, unlike ParM filaments, do not appear to disassemble catastrophically, and (ii) MamK filaments show a unique architecture in which interstrand monomers are in register and lack the staggered alignment typical of two-stranded actin filaments and most other characterized bacterial actins.

The study of bacterial actin MamK and its role in magnetotactic bacteria is an active area of research, and several groups have contributed, through both *in vivo* and *in vitro* studies, to progress in the field. In a brief report, Taoka *et al.* (25) demonstrated, for the first time, that recombinant MamK-His can form filamentous structures *in vitro*. Similar to the study by Toaka *et al.* (25) and later studies (26, 27), we show that MamK polymerizes into filaments *in vitro*. Despite this similarity, important differences exist between our study and previous work. MamK-His filament bundles could be visualized by EM after addition of ATPγS, a nonhydrolyzable ATP analog but, interestingly, not after addition of ATP. This suggested that MamK-His filaments disassembled prior to visualization due to ATP hydrolysis (25, 26). In stark contrast, Rioux *et al.* (27) reported that MamK-His polymerization occurred in the absence of nucleotide. The authors included ATP during the purification procedure and suggested that ATP, as it does for actin, stabilized MamK against aggregation. In contrast to previous studies, we demonstrate that the untagged MamK polymerizes in an ATP-dependent manner and that MamK filaments can be visualized by EM in the presence of this nucleotide. In addition to the above mentioned differences, our study contradicts findings with regard to the role of K^+ ions for MamK polymerization reported by Sonkaria *et al.* (26). The authors reported that MamK polymerization was inhibited in a K^+ concentration-dependent manner, with complete absence of polymerization at 200 mM KCl. As discussed later, under our experimental conditions MamK clearly polymerizes at similarly high KCl concentrations.

We can only speculate about the reasons for the different reported behaviors of MamK. A likely explanation is the use of slightly different MamK proteins in the different studies. Toaka *et al.* (25) and Sonkaria *et al.* (26) used MamK from the closely related organisms *M. magnetotacticum* MS-1 and *M. gryphiswaldense* MSR-1, respectively. However, the different MamK protein sequences are extremely similar, making it an unlikely reason for different *in vitro* properties. For instance, MamK from *M. magnetotacticum* MS-1 is 99% identical and 100% similar to its counterpart from AMB-1 studied here. It is important to note that Sonkaria *et al.* (26) expressed a slightly longer version of the MamK protein. In addition to the His tag at the C terminus, another 13 residues were expressed at the N terminus of the protein. These additional 13 residues are present in database entries for MamK from *M. gryphiswaldense* MSR-1 but are lacking in other MamK proteins. This longer protein was reported not to express functionally *in vivo* and thus may not be the correct MamK sequence (24). A further difference between our work and the previous studies is that we did not employ a His tag to purify MamK. Such tags could alter the protein's assembly and disassembly behavior. In fact, different properties have been reported for MreB from *T. maritima* purified either with or without a His tag (43, 58).

In vitro studies so far have only provided a static and limited picture of MamK assembly, and important questions about filament stability and architecture remain to be addressed. In this study, we investigated the dynamics of both MamK assembly and disassembly using light scattering assays. MamK filaments assemble rapidly in the presence of saturating levels of ATP. This is consistent with the behavior of other bacterial actins and may support the view that, in contrast to actin, bacterial actins do not require nucleation factors to promote efficient and rapid filament assembly. This filament assembly is not dependent on ATP hydrolysis as $MamK^{E143A}$, with its greatly reduced activity, still formed filaments. The $MamK^{E143A}$ data are consistent with the behavior of the well characterized bacterial actin ParM. Garner *et al.* (17) demonstrated that ParM with the equivalent mutation E148A is able to assemble into filaments but fails to exhibit any detectable ATPase activity. Although the $ParM^{E148A}$ protein assembles into filaments, the mutation renders these filaments stable as demonstrated in bulk by light scattering assays and at the single filament level using TIRF microscopy. The behavior of $MamK^{E143A}$ in light scattering experiments is consistent with the failure of filaments to disassemble and indicates that ATP hydrolysis is also important for

MamK filament disassembly. Moreover, this is in line with our previous work showing that MamK-GFP filament turnover in an *in vivo* fluorescence recovery after photobleaching assay is dependent on an intact nucleotide-binding site (19).

Our data also show that wild type MamK filament bulk disassembly occurs, at least in the presence of low potassium levels, relatively slowly. This disassembly behavior is different from ParM for which filament dynamics is best understood. ParM filaments exhibit dynamic instability where disassembly occurs rapidly and catastrophically. It is worth noting that MamK's ATPase activity, with 0.2 μM min^{-1}/μM protein, is significantly lower than for ParM (~3–6 μM min^{-1}/μM protein (17, 41), perhaps accounting for some aspects of the different time scales of filament dynamics. A direct comparison of MamK filament disassembly to that of ParM is difficult and requires the assessment of molecular events at the single MamK filament level. For instance, it is unknown if MamK filaments have a polarity to their growth and disassembly. It is possible that MamK filaments grow bidirectionally similar to ParM or that growth occurs preferentially from one end. Considering that MamK polymerizes readily with ATP but not ADP, it is conceptually possible that MamK filaments undergo a process of treadmilling similar to actin. Our attempts to analyze single MamK filaments using TIRF have proven difficult. This is mainly because labeling of MamK with biotin, required for immobilization of filaments on streptavidin functionalized glass slides when performing TIRF, is inefficient, and association of the labeled protein with the glass surface is poor. Furthermore, the length of fluorescently labeled (Alexa 488) MamK filaments is short and at the resolution limit for this type of microscopy. More intensive efforts are required to study MamK at the single filament level to ultimately understand MamK dynamics *in vivo*.

Studies with AMB-1 cells suggest that MamK filaments are intrinsically stable *in vivo* and rely on regulators for their dynamic behavior. Specifically, two redundant proteins encoded by genes of the so-called magnetosome gene island (MAI), namely MamJ and LimJ, appear to play a role in MamK dynamics *in vivo*. However, in the absence of other MAI genes, MamJ or LimJ is not sufficient to reconstitute MamK filament dynamics suggesting the presence of other factors (19). In addition to proteins that influence MamK dynamics, an interesting question concerns physico-chemical conditions, such as the concentration of various ions, inside the AMB-1 cells that might affect the *in vivo* behavior of MamK. K^+ ions play important roles in bacteria, where they are involved in cell turgor pressure maintenance (49, 59), enzyme activation (60, 61), and regulation of cytoplasmic pH (62, 63). For instance, in *E. coli* and *Bacillus* sp. cells K^+ is the major cytoplasmic cation with K^+ concentrations ranging roughly from 150 mM and reaching up to 650 mM depending on growth conditions and availability (49–53, 64). Our *in vitro* experiments show that increased K^+ concentrations result in the formation of tight MamK filament bundles that display little to no disassembly under ATP-limiting conditions. This high level of stability is not due to modulation of the protein's ATPase activity because similar amounts of P_i were released with high or low K^+ concentrations. Interestingly, the plasmid-segregating bacterial actin AlfA also shows filament bundling *in vitro*, but unlike MamK, high KCl concentrations are required to dissociate AlfA bundles, indicating that filament interactions occur through electrostatic interactions (44).

Interestingly, we also observed that Mg^{2+} ions can alter MamK filament stability by a mechanism that appears to be distinct from the K^+ effect mentioned above. In the presence of excess Mg^{2+}, we did not observe filament bundling. However, a reduction in ATPase activity, partially explaining the Mg^{2+}-dependent effect on filament stabilization, was seen. It is possible that MamK possesses a low affinity binding site for divalent cations that, when saturated, alters the filament in such a way that the off rate of MamK monomers is reduced. In *E. coli* free cytoplasmic Mg^{2+} levels have been estimated to be in the range of 2–4 mM (65, 66) making it plausible that the effects seen in these experiments may have physiological relevance.

It is yet unknown what levels of cytoplasmic K^+ AMB-1 cells maintain and how MamK filament bundling observed with increased K^+ levels *in vitro* relates to *in vivo* conditions. High resolution imaging by electron cryotomography on intact AMB-1 cells rather suggests that MamK forms single filaments *in vivo* (20). In wild type AMB-1 cells filaments of ~6 nm width, similar to the width of single filaments *in vitro*, run alongside of magnetosomes in the cytoplasm. Although some level of interfilament interactions, in the form of local overlaps, is seen *in vivo* (20), filament bundling to the extent that is seen under *in vitro* conditions is not observed. However, we previously observed *in vivo* bundling of putative MamK filaments between the gaps of the magnetosome chain that appear in mutant AMB-1 cells lacking the MamJ and LimJ proteins (19). One interpretation of these results has been that MamJ and LimJ contribute to the dynamics of MamK filaments by directly or indirectly affecting its ATPase activity. However, in light of our *in vitro* results, one could alternatively suggest that the lack of *in vivo* filament dynamics in the absence of MamJ and LimJ is a result of pronounced interfilament interactions and bundling. In this model, the absence of MamJ, or the redundant protein LimJ, would impair the proper interaction of magnetosomes with MamK filaments that are then free to associate with each other. Further support for this model comes from the observation that in the complete absence of magnetosomes in an MAI deletion mutant, a strain without any putative MamK anchorage points, MamK-GFP fluorescence no longer shows a typical linear, pole-to-pole localization but rather shows shorter and much thicker filaments. Furthermore, in this mutant MamK filaments are no longer dynamic, and together with the change in MamK filament organization this may hint toward MamK filament bundling in these cells.

Our structure of *in vitro* polymerized MamK reveals a novel architecture for an actin homolog. Although the surfaces of MamK involved in longitudinal contacts along each strand are similar to F-actin and other bacterial actin filaments, the cross-strand contacts are novel and lead to an unusual nonstaggered filament. Similar nonstaggered filament morphology has been observed for short filaments of MreB (13). In that case, the shape of the subunits in averaged images and arguments about how subunits interact with membranes suggested an antiparallel arrangement of the two MreB strands. The two strands of

MamK filaments, however, appear to be parallel to each other. The architecture of MamK filaments fits with a growing body of evidence that the broad diversity of bacterial actin filament morphologies arises primarily from variation in the cross-strand contacts, with similar surfaces utilized in forming longitudinal contacts along each strand (13, 44–46, 57, 67–69).

MamK's unique filament architecture poses interesting questions about its assembly, particularly at early stages requiring a nucleus for filament assembly. In staggered filaments, such as actin or ParM, once a trimer is formed, each subsequent subunit addition forms a new high affinity "corner" site where an incoming subunit can make both longitudinal and cross-strand contacts. Our preliminary analysis, by applying the Nishida and Sakai formalism (70), estimates the MamK nucleus size to be a trimer. For MamK, with unstaggered strands, a model involving a trimer as nucleus would, however, cause a conceptual problem. For MamK, a high affinity site could potentially exist when three subunits are assembled, but addition of a fourth subunit would yield a closed structure with no available corner sites, to which subunits would be added (supplemental Fig. S4*C*). It has to be noted that the Nishida and Sakai formalism may not strictly apply to MamK. More extensive work, involving both experimental and theoretical approaches, is required to answer questions revolving around MamK nucleus size and filament assembly.

Our study provides the first comprehensive view of MamK assembly behavior and filament architecture *in vitro*. As new regulators and interaction partners of MamK are discovered, this *in vitro* system will be an invaluable tool to decipher genetic and cell biological observations in a mechanistic light. The combination of these efforts should bring us closer to understanding the actual function of MamK in magnetosome alignment and division.

Acknowledgments—We thank Dyche Mullins and group members (University of California at San Francisco), in particular Jessica Polka and Scott Hansen, for providing guidance and access to equipment in the early stages of the project. We thank members of the Komeili laboratory for their critical reading of the manuscript. We extend our thanks to the Facility for Electron Microscopy Research at McGill University for the use of electron microscopes. We also thank Krishna Niyogi and Matthew Welch (University of California, Berkeley) for access to equipment.

REFERENCES

1. Cabeen, M. T., and Jacobs-Wagner, C. (2010) The bacterial cytoskeleton. *Annu. Rev. Genet.* **44,** 365–392
2. Ingerson-Mahar, M., and Gitai, Z. (2012) A growing family. The expanding universe of the bacterial cytoskeleton. *FEMS Microbiol. Rev.* **36,** 256–266
3. Shaevitz, J. W., and Gitai, Z. (2010) The structure and function of bacterial actin homologs. *Cold Spring Harbor Perspect. Biol.* **2,** a000364
4. Dominguez, R., and Holmes, K. C. (2011) Actin structure and function. *Annu. Rev. Biophys.* **40,** 169–186
5. Pollard, T. D., and Cooper, J. A. (2009) Actin, a central player in cell shape and movement. *Science* **326,** 1208–1212
6. Galkin, V. E., VanLoock, M. S., Orlova, A., and Egelman, E. H. (2002) A new internal mode in F-actin helps explain the remarkable evolutionary conservation of actin's sequence and structure. *Curr. Biol.* **12,** 570–575
7. Sheterline, P., Clayton, J., and Sparrow, J. (1995) Actin. *Protein Profile* **2,** 1–103
8. Derman, A. I., Becker, E. C., Truong, B. D., Fujioka, A., Tucey, T. M., Erb, M. L., Patterson, P. C., and Pogliano, J. (2009) Phylogenetic analysis identifies many uncharacterized actin-like proteins (Alps) in bacteria. Regulated polymerization, dynamic instability, and treadmilling in Alp7A. *Mol. Microbiol.* **73,** 534–552
9. Bork, P., Sander, C., and Valencia, A. (1992) An ATPase domain common to prokaryotic cell cycle proteins, sugar kinases, actin, and Hsp70 heat shock proteins. *Proc. Natl. Acad. Sci. U.S.A.* **89,** 7290–7294
10. Kabsch, W., and Holmes, K. C. (1995) The actin fold. *FASEB J.* **9,** 167–174
11. Jensen, R. B., and Gerdes, K. (1997) Partitioning of plasmid R1. The ParM protein exhibits ATPase activity and interacts with the centromere-like ParR-parC complex. *J. Mol. Biol.* **269,** 505–513
12. Jones, L. J., Carballido-López, R., and Errington, J. (2001) Control of cell shape in bacteria: helical, actin-like filaments in *Bacillus subtilis*. *Cell* **104,** 913–922
13. Salje, J., van den Ent, F., de Boer, P., and Löwe, J. (2011) Direct membrane binding by bacterial actin MreB. *Mol. Cell* **43,** 478–487
14. Domínguez-Escobar, J., Chastanet, A., Crevenna, A. H., Fromion, V., Wedlich-Söldner, R., and Carballido-López, R. (2011) Processive movement of MreB-associated cell wall biosynthetic complexes in bacteria. *Science* **333,** 225–228
15. Garner, E. C., Bernard, R., Wang, W., Zhuang, X., Rudner, D. Z., and Mitchison, T. (2011) Coupled, circumferential motions of the cell wall synthesis machinery and MreB filaments in *B. subtilis*. *Science* **333,** 222–225
16. van Teeffelen, S., Wang, S., Furchtgott, L., Huang, K. C., Wingreen, N. S., Shaevitz, J. W., and Gitai, Z. (2011) The bacterial actin MreB rotates, and rotation depends on cell-wall assembly. *Proc. Natl. Acad. Sci. U.S.A.* **108,** 15822–15827
17. Garner, E. C., Campbell, C. S., and Mullins, R. D. (2004) Dynamic instability in a DNA-segregating prokaryotic actin homolog. *Science* **306,** 1021–1025
18. Salje, J., Gayathri, P., and Löwe, J. (2010) The ParMRC system. Molecular mechanisms of plasmid segregation by actin-like filaments. *Nat. Rev. Microbiol.* **8,** 683–692
19. Draper, O., Byrne, M. E., Li, Z., Keyhani, S., Barrozo, J. C., Jensen, G., and Komeili, A. (2011) MamK, a bacterial actin, forms dynamic filaments *in vivo* that are regulated by the acidic proteins MamJ and LimJ. *Mol. Microbiol.* **82,** 342–354
20. Komeili, A., Li, Z., Newman, D. K., and Jensen, G. J. (2006) Magnetosomes are cell membrane invaginations organized by the actin-like protein MamK. *Science* **311,** 242–245
21. Bazylinski, D. A., and Frankel, R. B. (2004) Magnetosome formation in prokaryotes. *Nat. Rev. Microbiol.* **2,** 217–230
22. Jogler, C., and Schüler, D. (2009) Genomics, genetics, and cell biology of magnetosome formation. *Annu. Rev. Microbiol.* **63,** 501–521
23. Komeili, A. (2012) Molecular mechanisms of compartmentalization and biomineralization in magnetotactic bacteria. *FEMS Microbiol. Rev.* **36,** 232–255
24. Katzmann, E., Müller, F. D., Lang, C., Messerer, M., Winklhofer, M., Plitzko, J. M., and Schüler, D. (2011) Magnetosome chains are recruited to cellular division sites and split by asymmetric septation. *Mol. Microbiol.* **82,** 1316–1329
25. Taoka, A., Asada, R., Wu, L. F., and Fukumori, Y. (2007) Polymerization of the actin-like protein MamK, which is associated with magnetosomes. *J. Bacteriol.* **189,** 8737–8740
26. Sonkaria, S., Fuentes, G., Verma, C., Narang, R., Khare, V., Fischer, A., and Faivre, D. (2012) Insight into the assembly properties and functional organisation of the magnetotactic bacterial actin-like homolog, MamK. *PLoS ONE* **7,** e34189
27. Rioux, J. B., Philippe, N., Pereira, S., Pignol, D., Wu, L. F., and Ginet, N. (2010) A second actin-like MamK protein in *Magnetospirillum magneticum* AMB-1 encoded outside the genomic magnetosome island. *PLoS ONE* **5,** e9151
28. Ohi, M., Li, Y., Cheng, Y., and Walz, T. (2004) Negative staining and image classification–Powerful tools in modern electron microscopy. *Biol. Proced. Online* **6,** 23–34

29. Mindell, J. A., and Grigorieff, N. (2003) Accurate determination of local defocus and specimen tilt in electron microscopy. *J. Struct. Biol.* **142,** 334–347
30. Ludtke, S. J., Baldwin, P. R., and Chiu, W. (1999) EMAN. Semiautomated software for high resolution single-particle reconstructions. *J. Struct. Biol.* **128,** 82–97
31. Egelman, E. H. (2007) The iterative helical real space reconstruction method. Surmounting the problems posed by real polymers. *J. Struct. Biol.* **157,** 83–94
32. Sachse, C., Chen, J. Z., Coureux, P. D., Stroupe, M. E., Fändrich, M., and Grigorieff, N. (2007) High-resolution electron microscopy of helical specimens: a fresh look at tobacco mosaic virus. *J. Mol. Biol.* **371,** 812–835
33. Frank, J. (ed) (1996) *Three-dimensional Electron Microscopy of Macromolecular Assemblies*, pp. 1–342, Academic Press, Inc., San Diego
34. Egelman, E. H. (2000) A robust algorithm for the reconstruction of helical filaments using single-particle methods. *Ultramicroscopy* **85,** 225–234
35. Behrmann, E., Tao, G., Stokes, D. L., Egelman, E. H., Raunser, S., and Penczek, P. A. (2012) Real-space processing of helical filaments in SPARX. *J. Struct. Biol.* **177,** 302–313
36. Pettersen, E. F., Goddard, T. D., Huang, C. C., Couch, G. S., Greenblatt, D. M., Meng, E. C., and Ferrin, T. E. (2004) UCSF Chimera–a visualization system for exploratory research and analysis. *J. Comput. Chem.* **25,** 1605–1612
37. van den Ent, F., Amos, L. A., and Löwe, J. (2001) Prokaryotic origin of the actin cytoskeleton. *Nature* **413,** 39–44
38. Fiser, A., and Sali, A. (2003) Modeller: generation and refinement of homology-based protein structure models. *Methods Enzymol.* **374,** 461–491
39. Altschul, S. F., Gish, W., Miller, W., Myers, E. W., and Lipman, D. J. (1990) Basic local alignment search tool. *J. Mol. Biol.* **215,** 403–410
40. Katoh, K., Misawa, K., Kuma, K., and Miyata, T. (2002) MAFFT. A novel method for rapid multiple sequence alignment based on fast Fourier transform. *Nucleic Acids Res.* **30,** 3059–3066
41. Rivera, C. R., Kollman, J. M., Polka, J. K., Agard, D. A., and Mullins, R. D. (2011) Architecture and assembly of a divergent member of the ParM family of bacterial actin-like proteins. *J. Biol. Chem.* **286,** 14282–14290
42. Vorobiev, S., Strokopytov, B., Drubin, D. G., Frieden, C., Ono, S., Condeelis, J., Rubenstein, P. A., and Almo, S. C. (2003) The structure of nonvertebrate actin: implications for the ATP hydrolytic mechanism. *Proc. Natl. Acad. Sci. U.S.A.* **100,** 5760–5765
43. Bean, G. J., and Amann, K. J. (2008) Polymerization properties of the *Thermotoga maritima* actin MreB. Roles of temperature, nucleotides, and ions. *Biochemistry* **47,** 826–835
44. Polka, J. K., Kollman, J. M., Agard, D. A., and Mullins, R. D. (2009) The structure and assembly dynamics of plasmid actin AlfA imply a novel mechanism of DNA segregation. *J. Bacteriol.* **191,** 6219–6230
45. Popp, D., Narita, A., Lee, L. J., Ghoshdastider, U., Xue, B., Srinivasan, R., Balasubramanian, M. K., Tanaka, T., and Robinson, R. C. (2012) Novel actin-like filament structure from *Clostridium tetani*. *J. Biol. Chem.* **287,** 21121–21129
46. Popp, D., Xu, W., Narita, A., Brzoska, A. J., Skurray, R. A., Firth, N., Ghoshdastider, U., Goshdastider, U., Maéda, Y., Robinson, R. C., and Schumacher, M. A. (2010) Structure and filament dynamics of the pSK41 actin-like ParM protein. Implications for plasmid DNA segregation. *J. Biol. Chem.* **285,** 10130–10140
47. Esue, O., Wirtz, D., and Tseng, Y. (2006) GTPase activity, structure, and mechanical properties of filaments assembled from bacterial cytoskeleton protein MreB. *J. Bacteriol.* **188,** 968–976
48. Wen, K. K., Yao, X., and Rubenstein, P. A. (2002) GTP-yeast actin. *J. Biol. Chem.* **277,** 41101–41109
49. Epstein, W., and Schultz, S. G. (1965) Cation transport in *Escherichia coli*: V. Regulation of cation content. *J. Gen. Physiol.* **49,** 221–234
50. Jahns, T. (1994) Ammonium-stimulated, sodium-dependent uptake of glutamine in *Bacillus pasteurii*. *Arch. Microbiol.* **161,** 207–214
51. McLaggan, D., Naprstek, J., Buurman, E. T., and Epstein, W. (1994) Interdependence of K^+ and glutamate accumulation during osmotic adaptation of *Escherichia coli*. *J. Biol. Chem.* **269,** 1911–1917
52. Michels, M., and Bakker, E. P. (1987) Low-affinity potassium uptake system in *Bacillus acidocaldarius*. *J. Bacteriol.* **169,** 4335–4341
53. Roe, A. J., McLaggan, D., O'Byrne, C. P., and Booth, I. R. (2000) Rapid inactivation of the *Escherichia coli* Kdp K^+ uptake system by high potassium concentrations. *Mol. Microbiol.* **35,** 1235–1243
54. Galkin, V. E., Orlova, A., Schröder, G. F., and Egelman, E. H. (2010) Structural polymorphism in F-actin. *Nat. Struct. Mol. Biol.* **17,** 1318–1323
55. Murakami, K., Yasunaga, T., Noguchi, T. Q., Gomibuchi, Y., Ngo, K. X., Uyeda, T. Q., and Wakabayashi, T. (2010) Structural basis for actin assembly, activation of ATP hydrolysis, and delayed phosphate release. *Cell* **143,** 275–287
56. Fujii, T., Iwane, A. H., Yanagida, T., and Namba, K. (2010) Direct visualization of secondary structures of F-actin by electron cryomicroscopy. *Nature* **467,** 724–728
57. Galkin, V. E., Orlova, A., Rivera, C., Mullins, R. D., and Egelman, E. H. (2009) Structural polymorphism of the ParM filament and dynamic instability. *Structure* **17,** 1253–1264
58. Esue, O., Cordero, M., Wirtz, D., and Tseng, Y. (2005) The assembly of MreB, a prokaryotic homolog of actin. *J. Biol. Chem.* **280,** 2628–2635
59. Whatmore, A. M., and Reed, R. H. (1990) Determination of turgor pressure in *Bacillus subtilis*. A possible role for K^+ in turgor regulation. *J. Gen. Microbiol.* **136,** 2521–2526
60. Rosen, B. P., and Silver, S. (eds) (1987) *Ion Transport in Prokaryotes*, pp. 85–114, Academic Press, San Diego
61. Suelter, C. H. (1970) Enzymes activated by monovalent cations. *Science* **168,** 789–795
62. Booth, I. R. (1985) Regulation of cytoplasmic pH in bacteria. *Microbiol. Rev.* **49,** 359–378
63. Kroll, R. G., and Booth, I. R. (1983) The relationship between intracellular pH, the pH gradient and potassium transport in *Escherichia coli*. *Biochem. J.* **216,** 709–716
64. López, D., Fischbach, M. A., Chu, F., Losick, R., and Kolter, R. (2009) Structurally diverse natural products that cause potassium leakage trigger multicellularity in *Bacillus subtilis*. *Proc. Natl. Acad. Sci. U.S.A.* **106,** 280–285
65. Alatossava, T., Jütte, H., Kuhn, A., and Kellenberger, E. (1985) Manipulation of intracellular magnesium content in polymyxin B nonapeptide-sensitized *Escherichia coli* by ionophore A23187. *J. Bacteriol.* **162,** 413–419
66. Lusk, J. E., Williams, R. J., and Kennedy, E. P. (1968) Magnesium and the growth of *Escherichia coli*. *J. Biol. Chem.* **243,** 2618–2624
67. Orlova, A., Garner, E. C., Galkin, V. E., Heuser, J., Mullins, R. D., and Egelman, E. H. (2007) The structure of bacterial ParM filaments. *Nat. Struct. Mol. Biol.* **14,** 921–926
68. Roeben, A., Kofler, C., Nagy, I., Nickell, S., Hartl, F. U., and Bracher, A. (2006) Crystal structure of an archaeal actin homolog. *J. Mol. Biol.* **358,** 145–156
69. Szwedziak, P., Wang, Q., Freund, S. M., and Lowe, J. (2012) FtsA forms actin-like protofilaments. *EMBO J.* **31,** 2249–2260
70. Nishida, E., and Sakai, H. (1983) Kinetic analysis of actin polymerization. *J. Biochem.* **93,** 1011–1020

The bacterial actin MamK: *in vitro* assembly behavior and filament architecture

SUPPLEMENTARY INFORMATION

Ertan Ozyamak, Justin Kollman, David A. Agard, Arash Komeili

SUPPLEMENTARY FIGURE LEGENDS

FIGURE S1. Wild type MamK and mutant E143A proteins can be obtained at high purity. A. Protein was purified employing the routine procedure described in Experimental procedures. Coomassie stained 12% Laemmli gel is shown and protein loading is indicated above lanes. B. EDTA-treatment aids in the disassembly of MamK filaments. MamK polymerization was assessed by pelleting assays as described in Experimental procedures (supernatant fractions are shown). MamK, in polymerization buffer (see Experimental procedures) including 5 mM $MgCl_2$, was polymerized through addition of 5 mM ATP (sample 2); only buffer was added to control reaction without ATP (sample 1). A fraction of the total samples were analyzed by pelleting assay. Remainder of both samples were extensively dialyzed at 4°C against the buffer above (10,000 X sample volume) or buffer without 5 mM $MgCl_2$ but with 5 mM EDTA. Depolymerized protein (red box) was dialyzed into polymerization buffer with 5 mM $MgCl_2$ and re-polymerized with 5 mM ATP.

FIGURE S2. Polymerization of MamK at a low protein concentration. Illustration of data in Fig. 2A for 1.95 μM MamK over an extended period of time. Data show that at this low protein concentration MamK assembly kinetics follow a sigmoidal function.

FIGURE S3. Determination of MamK critical concentration by light scattering. Plot of maximal light scattering intensities against various initial protein concentrations. x-intercept of linear fit provides extrapolation of critical concentration. A-C. Plots were generated using same data as in Fig. 2A-C. D. Plot for data of MamK polymerization in buffer with 75 mM KCl.

FIGURE S4. Estimation of MamK nucleus size. According to the Nishida & Sakai formalism the nucleus size can be estimated from a plot of maximal velocity of light scattering traces (V_{max}), divided by the maximal intensity (I_{max}), against the log protein concentrations. The nucleus size is estimated as two times the slope of the linear fit. Same data set as in Fig. 2 were used for analysis. Shown are plots for wild type MamK (A) and $MamK^{E143A}$ proteins (B). By this estimate the nucleus size for mutant E143A is a trimer. This analysis for the wild type protein only yields a linear relationship if polymerization at ~2 μM is not considered in the data analysis. This may indicate that the Nishida & Sakai formalism does not strictly apply to MamK or that polymerization at lower protein concentrations obeys a different mechanism. C. Models for MamK assembly.

FIGURE S5. Correlation between MamK polymerization and ATP hydrolysis / P_i release. MamK's ATPase activity was inferred by measuring P_i released during the assay as described in Experimental Procedures. 9.52 μM wild type MamK (black lines) and $MamK^{E143A}$ protein (gray lines) were polymerized in the presence of 50 μM ATP-$MgCl_2$. Data highlight that polymerization is independent of ATP hydrolysis / P_i release. Each trace is the average of three

measurements on the same day. Polymerization by light scattering (circles) was measured on the same day as P_i release.

FIGURE S6. Substoichiometric levels of mutant $MamK^{E143A}$ can stabilize wild type MamK filaments. A. $MamK^{E143A}$ protein (~2.5 or 5%) was spiked to ~ 9.52 μM wild type MamK protein and mixtures polymerized by addition of 25 μM ATP-$MgCl_2$. Presence of even ~2.5 % $MamK^{E143A}$ protein can significantly decrease bulk depolymerization rates of wild type filaments. Each trace is the average of two measurements on the same day. B. Varying levels of wild type and mutant protein were mixed whereby the total protein concentration in the reaction was kept at 9.52 μM. Polymerization was initiated by addition of 25 μM ATP-$MgCl_2$. Each trace is the average of two measurements on the same day.

FIGURE S7. P_i release in the presence of higher potassium levels. P_i release experiments were measured for 9.52 μM MamK after polymerization with either 2 mM (A) or 25 μM ATP-$MgCl_2$ - (B). P_i release assays were performed on the same day as light scattering assays shown in Fig. 5. Inset in (A) illustrates P_i release during early time points of experiments.

FIGURE S8. MamK polymerizes with slower kinetics in the presence of sodium chloride. Light scattering intensities were assessed for 9.52 μM MamK after polymerization with either 2 mM (A) or 500 μM ATP-$MgCl_2$ (B). MamK polymerization showed either a slower initial rate of polymerization (A) or a long lag phase (B) in the presence of 25 mM sodium chloride. Increased sodium levels rescued this to some extent. No polymerization was seen with 25 μM ATP-$MgCl_2$ (data not shown). C,D. P_i release assays, performed on the same day as light scattering assays in A and B respectively, show the reduced MamK ATPase activity in the presence sodium chloride. For all experiments, the buffer components were identical apart from varied KCl and NaCl levels. Each trace is the average of three measurements on the same day.

FIGURE S9. Mg^{2+} levels influence MamK filament stability and phosphate release. Light scattering intensities were assessed for 9.52 μM MamK after polymerization with 50 μM ATP and varying levels of $MgCl_2$. P_i release assays, were performed on the same day as light scattering assays in A and B, and show the reduced MamK ATPase activity in the presence of 100-fold excess $MgCl_2$. Each trace is the average of three measurements on the same day.

FIGURE S10. Verification of MamK filament structure and symmetry. A. Reference-free averages of MamK segments. MamK filament were extracted from cryo-EM micrographs in segments of ~480 Å, and binned four-fold to a pixel size of 3.76 Å/pixel. The segments were aligned and grouped into reference-free averaged with the startnrclasses routine of the EMAN software suite. The averages indicate that the two strands of the MamK filament are in register with each other, rather than staggered as in other actin-like protein filaments. B. MamK strands are parallel in the filament. Reconstructions were run enforcing different symmetry between the strands: i) antiparallel symmetry, ii) no symmetry, and iii) parallel symmetry (C2 point group symmetry axis coincident with the helix axis). When antiparallel symmetry is enforced, the well-defined subunit features are lost. With no point group symmetry the reconstruction develops quasi-two-fold parallel symmetry and retains well-defined subunit features, indicating that parallel symmetry should be imposed. Note that in all the reconstructions helical symmetry was imposed throughout, and each reconstruction converged on similar helical symmetry parameters (~23.4° azimuthal angle and ~53.0 Å axial rise). C. Convergence of helical symmetry parameters from different starting symmetries. Independent reconstructions were run with three different initial values of $\Delta\varphi$, the azimuthal rotation between adjacent helical subunits. Through multiple refinement rounds the values stably converge to 23.3° per subunit, indicating a correct solution to

the helical symmetry. Small variations in the azimuthal angle after convergence (~0.1°) may indicate a limited degree of heterogeneity in the helical symmetry. D. Resolution estimate for the MamK cryo-EM reconstruction. The Fourier Shell Correlation (FSC) was calculated between two volumes generated from half the entire data set. The resolution of the reconstruction is 12 Å by the FSC0.5 criterion.

FIGURE S11. Comparison of helical symmetry contacts among actin and actin-like filaments. Three subunits are shown for the actin (PDB:3MFP), and R1 ParM (PDB:3IKU) filament structures, along with four subunits from the MamK filament reconstruction. The helical twist from one subunit to the next along each strand is indicated below. Note that actin is a right-handed helix and ParM is left-handed; while we did not determine the absolute hand for the MamK helix, the MamK homology model fits best into the right-handed model. In both the actin and ParM filaments there is a half-subunit stagger between strands, whereas the two strands are in register in the MamK filament, resulting in two-fold point-group symmetry between the strands.

Figure S1

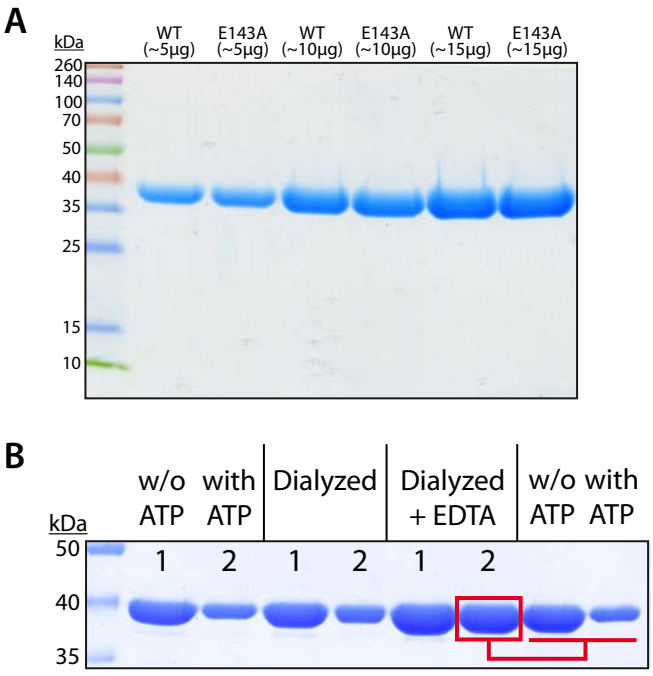
A
kDa
WT (~5µg)
E143A (~5µg)
WT (~10µg)
E143A (~10µg)
WT (~15µg)
E143A (~15µg)
260
140
100
70
50
40
35
25
15
10
B
kDa
w/o ATP
with ATP
Dialyzed
Dialyzed + EDTA
w/o ATP
with ATP
1
2
1
2
1
2
50
40
35

Figure S2

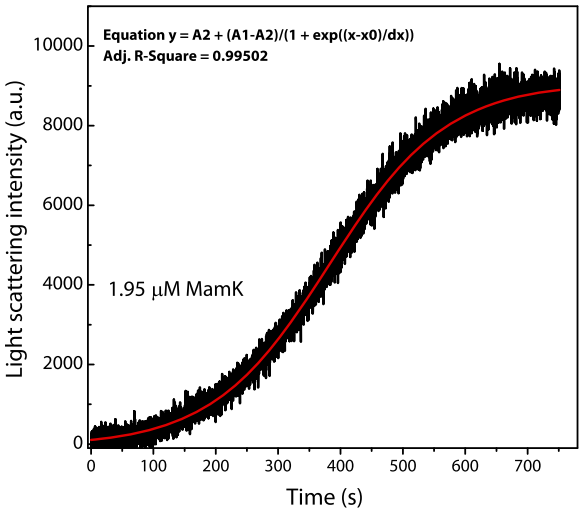
Equation y = A2 + (A1-A2)/(1 + exp((x-x0)/dx))
Adj. R-Square = 0.99502
1.95 μM MamK
Light scattering intensity (a.u.)
Time (s)
0
2000
4000
6000
8000
10000
0
100
200
300
400
500
600
700

Figure S3

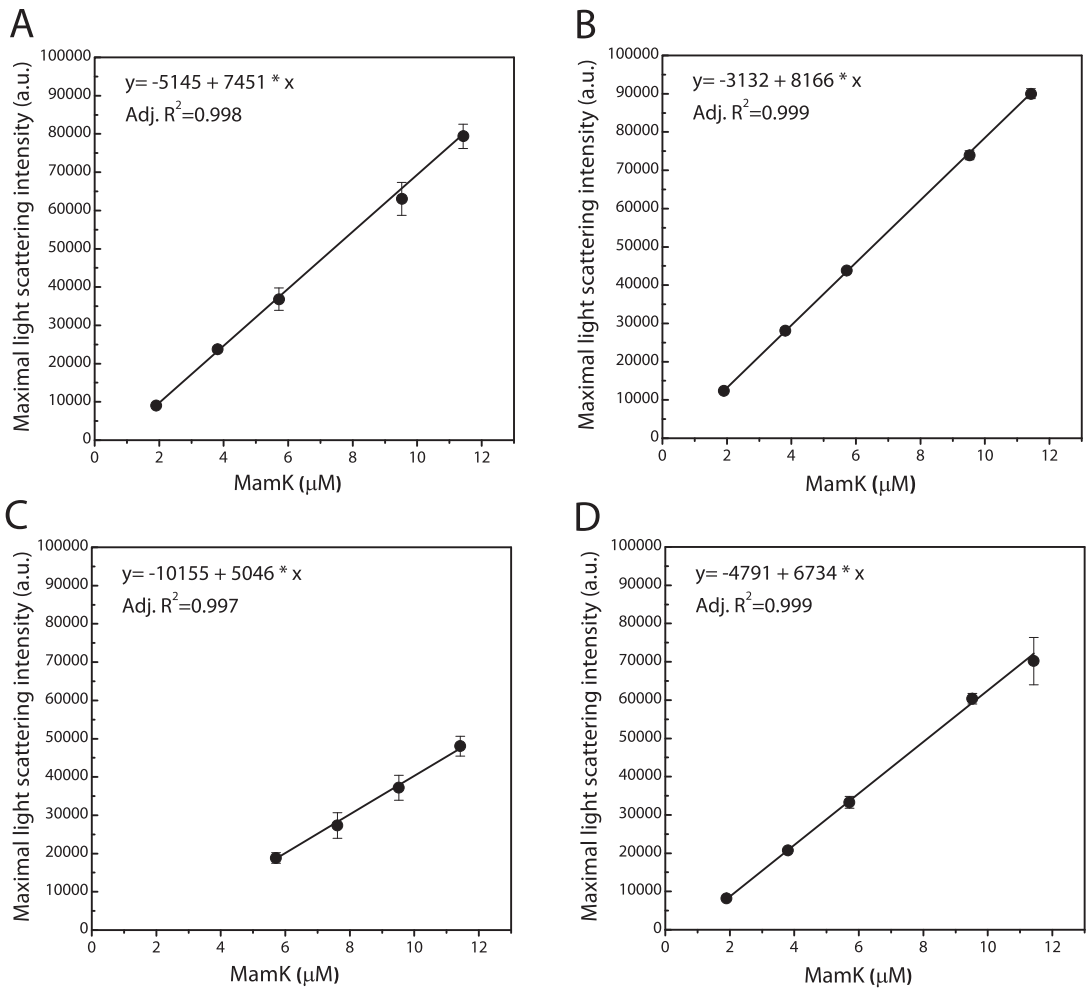
A
y= -5145 + 7451 * x
Adj. R2=0.998
B
y= -3132 + 8166 * x
Adj. R2=0.999
C
y= -10155 + 5046 * x
Adj. R2=0.997
D
y= -4791 + 6734 * x
Adj. R2=0.999
Maximal light scattering intensity (a.u.)
MamK (μM)

Figure S4

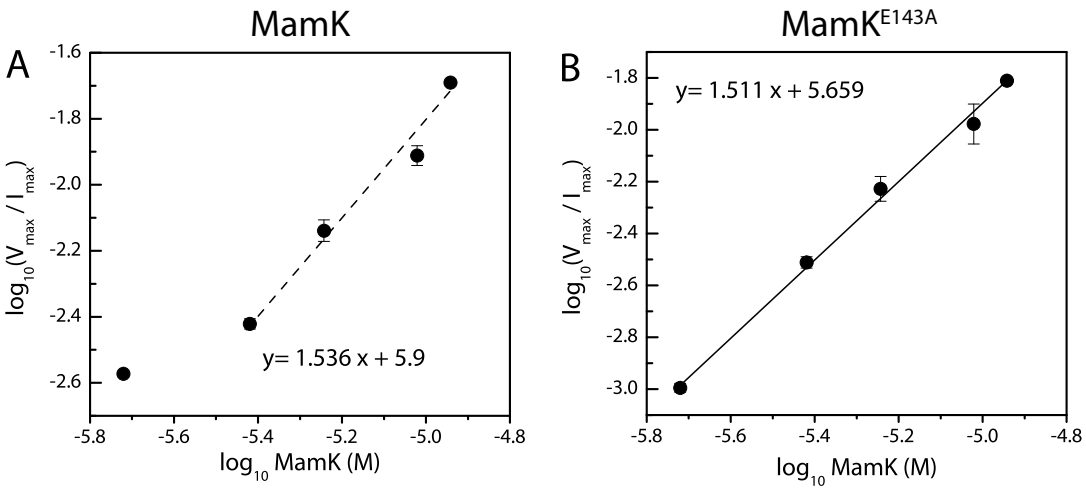
MamK
A
-1.6
-1.8
-2.0
-2.2
-2.4
-2.6
log10(Vmax / Imax)
y= 1.536 x + 5.9
-5.8
-5.6
-5.4
-5.2
-5.0
-4.8
log10 MamK (M)
MamKE143A
B
-1.8
-2.0
-2.2
-2.4
-2.6
-2.8
-3.0
y= 1.511 x + 5.659
log10(Vmax / Imax)
-5.8
-5.6
-5.4
-5.2
-5.0
-4.8
log10 MamK (M)

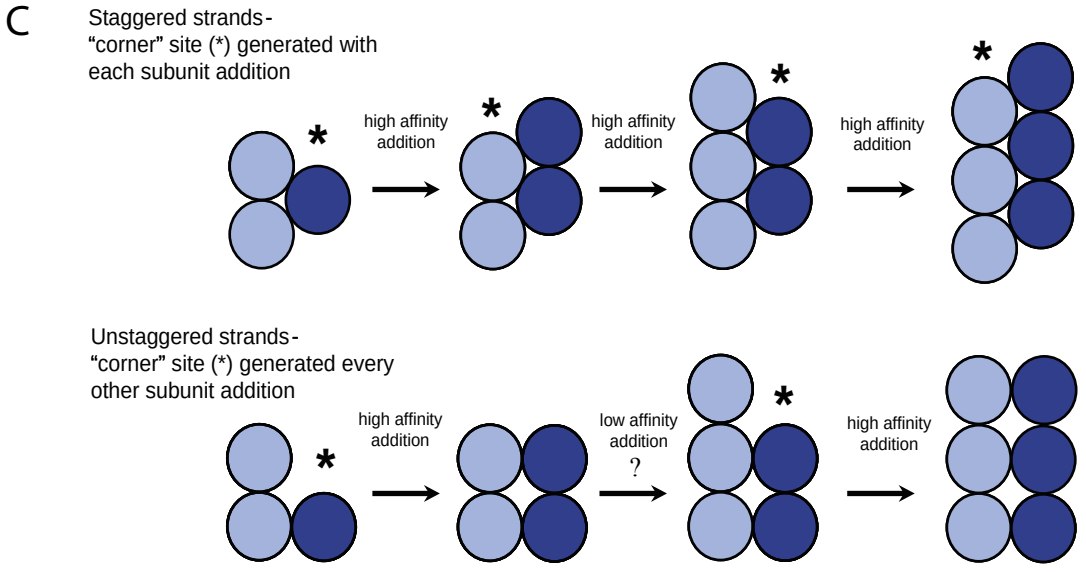
C
Staggered strands-
"corner" site (*) generated with
each subunit addition
high affinity
addition
high affinity
addition
high affinity
addition
Unstaggered strands-
"corner" site (*) generated every
other subunit addition
high affinity
addition
low affinity
addition
?
high affinity
addition

Figure S5

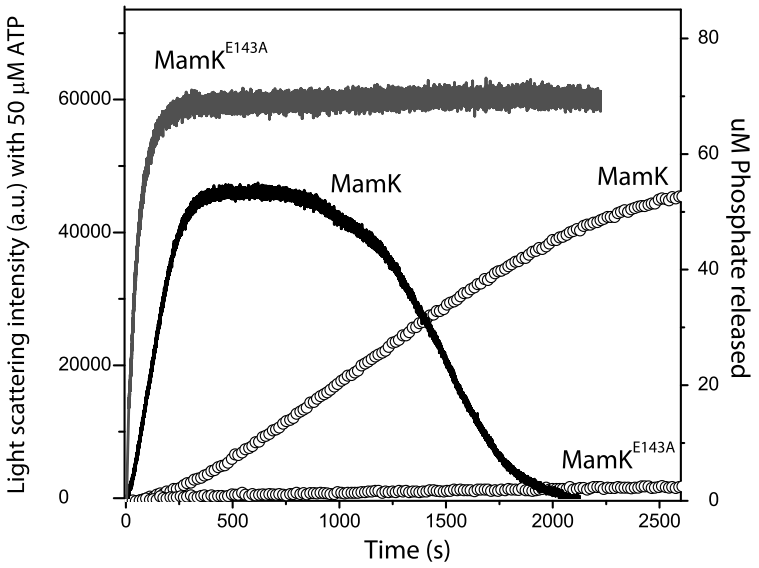
MamK^E143A
MamK
MamK
MamK^E143A
Light scattering intensity (a.u.) with 50 μM ATP
uM Phosphate released
Time (s)
0
20000
40000
60000
0
20
40
60
80
0
500
1000
1500
2000
2500

Figure S6

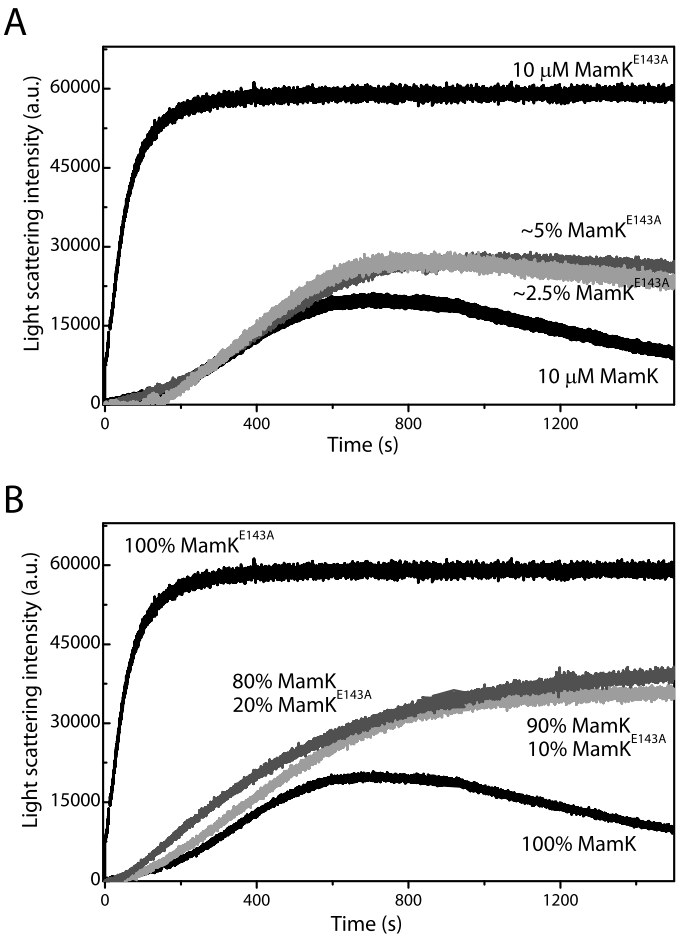
A
10 μM MamK^{E143A}
~5% MamK^{E143A}
~2.5% MamK^{E143A}
10 μM MamK
Light scattering intensity (a.u.)
60000
45000
30000
15000
0
0
400
800
1200
Time (s)
B
100% MamK^{E143A}
80% MamK
20% MamK^{E143A}
90% MamK
10% MamK^{E143A}
100% MamK
Light scattering intensity (a.u.)
60000
45000
30000
15000
0
0
400
800
1200
Time (s)

Figure S7

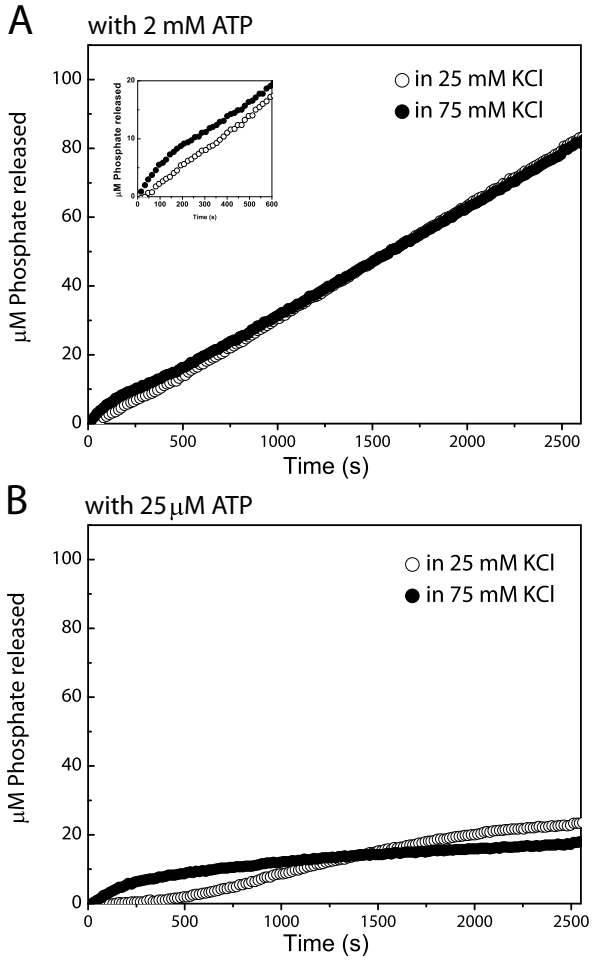
A
with 2 mM ATP
○ in 25 mM KCl
● in 75 mM KCl
μM Phosphate released
Time (s)
B
with 25μM ATP
○ in 25 mM KCl
● in 75 mM KCl
μM Phosphate released
Time (s)

Figure S8

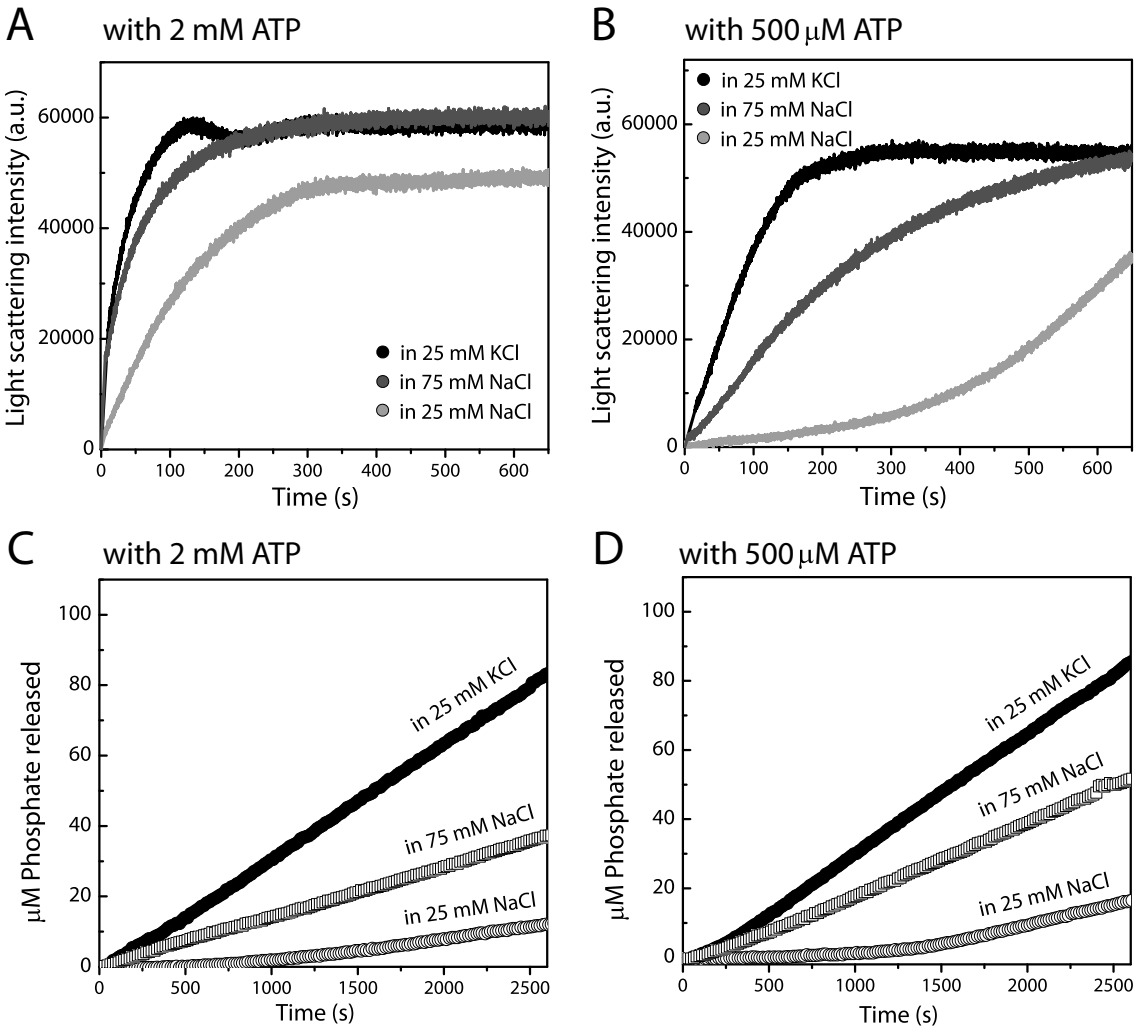
A
with 2 mM ATP
Light scattering intensity (a.u.)
Time (s)
in 25 mM KCl
in 75 mM NaCl
in 25 mM NaCl
B
with 500 μM ATP
Light scattering intensity (a.u.)
Time (s)
in 25 mM KCl
in 75 mM NaCl
in 25 mM NaCl
C
with 2 mM ATP
μM Phosphate released
Time (s)
in 25 mM KCl
in 75 mM NaCl
in 25 mM NaCl
D
with 500 μM ATP
μM Phosphate released
Time (s)
in 25 mM KCl
in 75 mM NaCl
in 25 mM NaCl

Figure S9

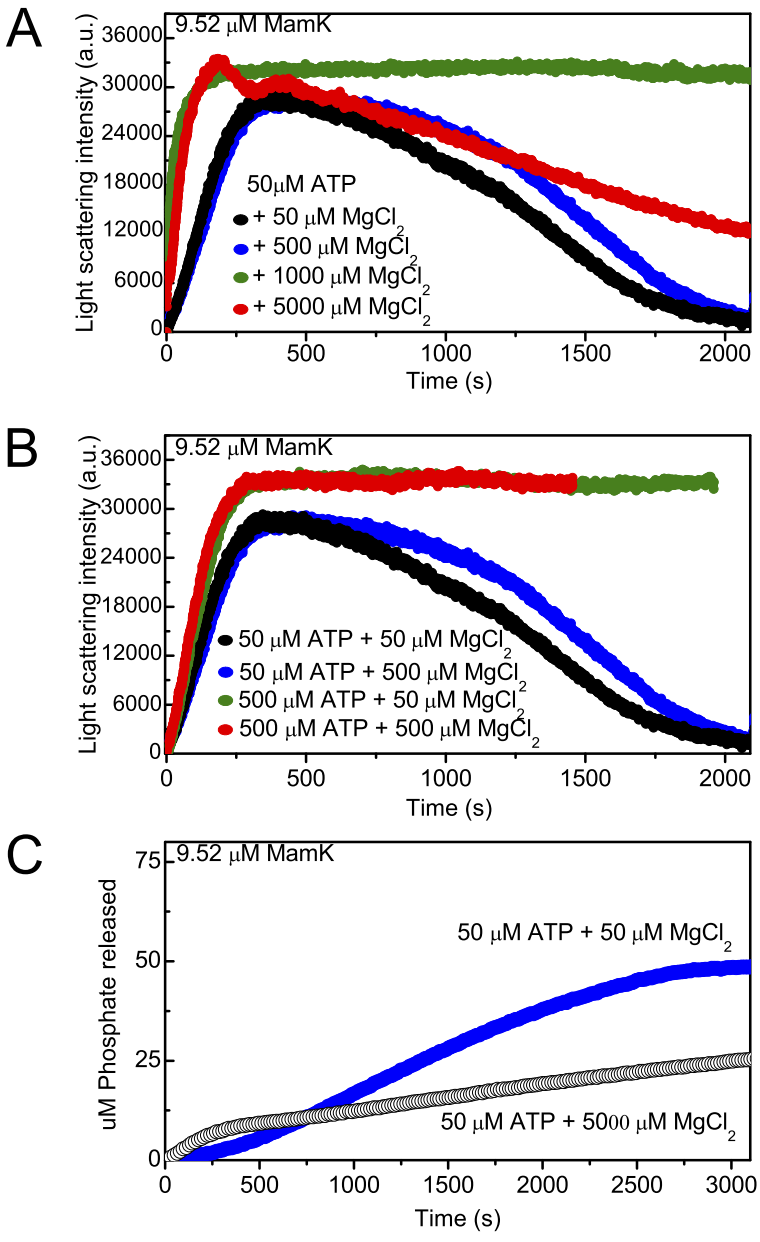
A
9.52 μM MamK
Light scattering intensity (a.u.)
36000
30000
24000
18000
12000
6000
0
50μM ATP
+ 50 μM MgCl2
+ 500 μM MgCl2
+ 1000 μM MgCl2
+ 5000 μM MgCl2
0
500
1000
1500
2000
Time (s)
B
9.52 μM MamK
Light scattering intensity (a.u.)
50 μM ATP + 50 μM MgCl2
50 μM ATP + 500 μM MgCl2
500 μM ATP + 50 μM MgCl2
500 μM ATP + 500 μM MgCl2
Time (s)
C
9.52 μM MamK
uM Phosphate released
75
50
25
0
50 μM ATP + 50 μM MgCl2
50 μM ATP + 5000 μM MgCl2
2500
3000
Time (s)

Figure S10

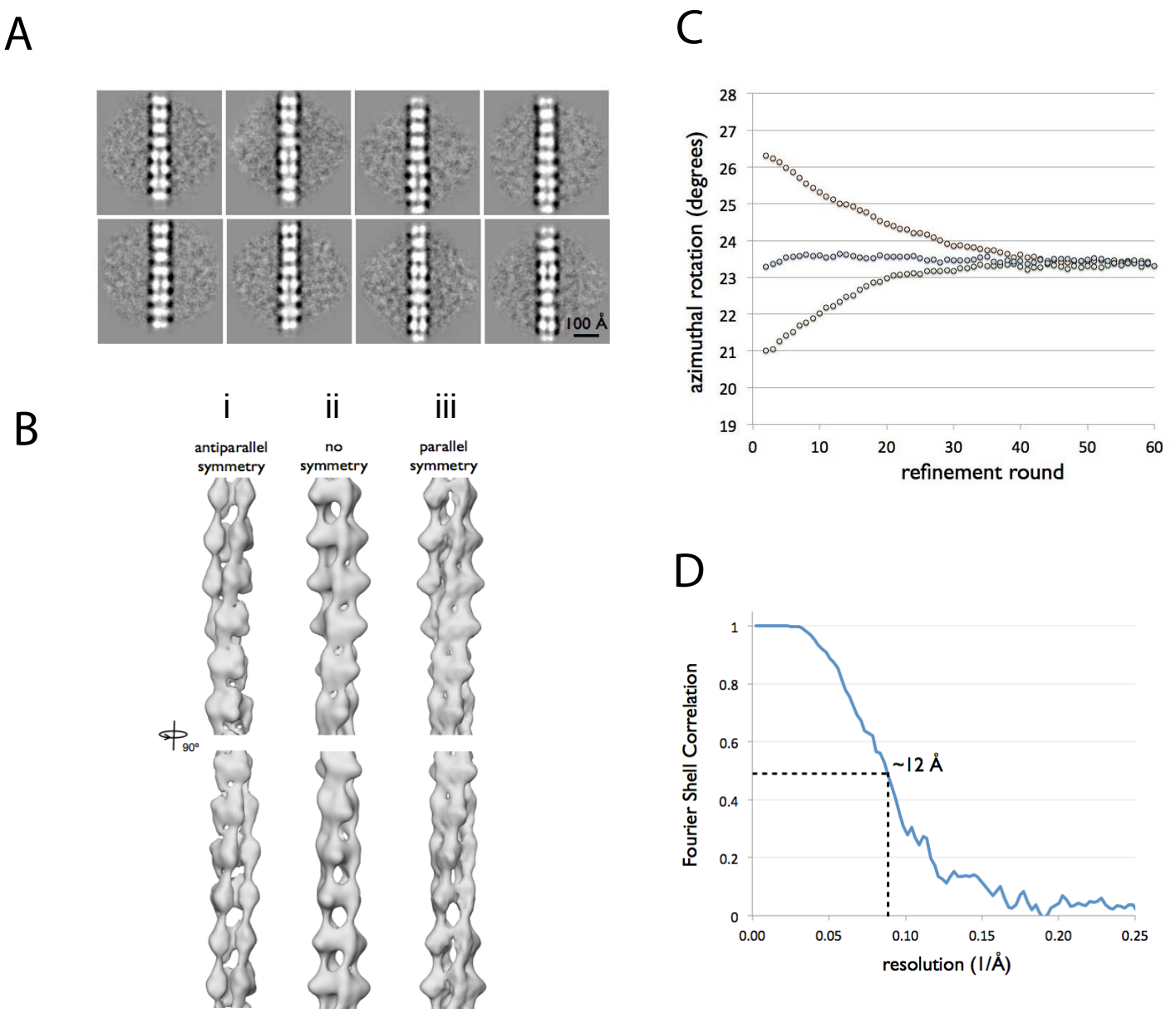
A
100 Å
B
i
ii
iii
antiparallel symmetry
no symmetry
parallel symmetry
90°
C
azimuthal rotation (degrees)
refinement round
D
Fourier Shell Correlation
~12 Å
resolution (1/Å)

Figure S11